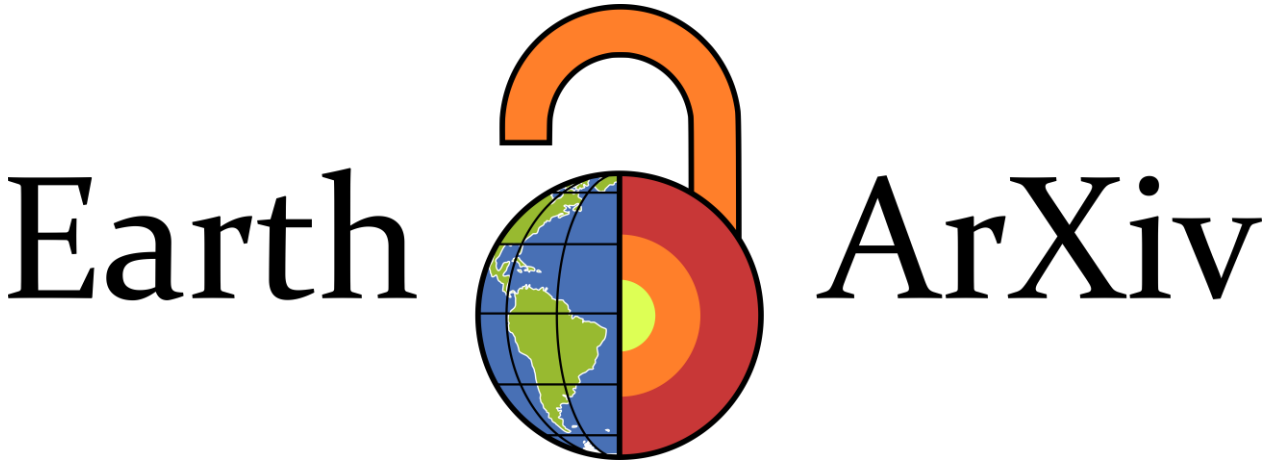

18 **Calcium promotes carbon rich grassland soils**

19 Slessarev, E.W.,[1,2*] Goertzen, H.R.,[3] Lybrand, R.,[3] McFarlane, K.J.,[4] Pett-Ridge, J.[4,5,6], Sokol,
20 N.[4], Zaharescu, D.[3] Georgiou, K.,[7]
21
22 [1] Department of Ecology and Evolutionary Biology, Yale University, New Haven, CT, USA
23 [2] Yale Center for Natural Carbon Capture, Yale University, New Haven, CT, USA
24 [3] Department of Land Air and Water Resources, University of California, Davis, CA, USA
25 [4] Physical and Life Sciences Directorate, Lawrence Livermore National Laboratory, Livermore,
26 CA, USA
27 [5] Innovative Genomics Institute, University of California Berkeley, Berkeley, CA, USA
28 [6] Life & Environmental Sciences Department, University of California Merced, Merced, CA,
29 USA
30 [7] Department of Biological and Ecological Engineering, Oregon State University, Corvallis, OR,
31 USA
32
33 *Corresponding author: eric.slessarev@yale.edu

34

Abstract

Dark colored grassland soils, known as Mollisols, are intensively farmed and exceptionally rich in organic matter, and hence have an important role in the carbon cycle. Storage of soil organic carbon (SOC) in Mollisols may result from interactions between organic matter and calcium (Ca) released by carbonate and silicate weathering. This synergy between SOC and Ca cycling has yet to be tested at scale. To close this knowledge gap, we developed a novel geochemical model and leveraged continental-scale datasets to simulate Ca release in soils across the USA. We found that Ca released by mineral weathering is associated with SOC storage and that this effect is stronger in Mollisols than in non-Mollisols. Our model also shows that agriculture has increased Ca inputs to cultivated USA Mollisols 5-6 fold, indicating that humans have fundamentally changed the geochemical conditions that sustain SOC in these soils. By implication, moderating the quantity of and timing of Ca release may help to preserve and restore SOC in the world's most intensively farmed landscapes.

Main

Temperate grasslands feature exceptionally fertile, dark-colored soils known as Mollisols. Mollisols are the world's most intensively farmed soil type.[1] Based on recent data,[2,3] we estimate that Mollisols comprise only 7% of the Earth's land area yet support 24% of agricultural land and 32% of all calories from production of corn, soy, and wheat. Mollisols also contribute disproportionately to soil organic carbon (SOC) storage, containing 32% of the organic C held in Earth's agricultural soils (see Methods). This makes Mollisols critical to land-based climate mitigation efforts. At the same time, Mollisols are disproportionately exposed to environmental threats, including soil erosion,[4] and have lost a significant fraction of their SOC to cultivation.[5] Effective stewardship of Mollisols in the face of these threats requires a comprehensive understanding of the environmental factors that make them fertile and C rich.

There are several ecological processes that contribute to the C richness of Mollisols, and these have implications for protecting and restoring SOC. As early as the 1860's, grassland vegetation was identified as the main driver of Mollisol formation.[6] Perennial grasses grow extensive fibrous root systems, and root turnover is an important pathway of SOC accrual.[7,8] Grasslands and savannas are characterized by frequent fires, and fires can generate persistent pyrogenic C that might explain the origin of Mollisols.[9] Grasslands also support robust populations of burrowing animals that help to engineer to the thick, C-rich topsoil layers characteristic of Mollisols.[10] Contemporary proposals for restoring SOC storage in cropland soils mimic ecological processes that are thought to be important in Mollisols. For instance, C sequestration might be achieved by returning deep rooted cultivars to croplands,[11] increasing plant diversity,[12] or amending soils with pyrogenic C.[13]

Geologic factors can also help to explain the C richness of Mollisols. Mollisols are commonly formed from calcareous rocks or from aeolian deposits rich in calcium carbonate.[6] Mollisols are, by definition, enriched in exchangeable Ca^{2+} and other base cations (Mg^{2+}, K^{+}, and Na^{+}).[14] A growing body of evidence shows that Ca stabilizes SOC. Ca facilitates sorption of organic molecules on clays and promotes the growth of bacterial biofilms that are retained on mineral surfaces.[15–17] These processes manifest at continental scales, where SOC is spatially correlated with exchangeable Ca^{2+}, i.e., Ca that is reversibly bound to surfaces as an exchangeable cation.[18,19] Exchangeable Ca^{2+} may directly link organic matter to minerals via cation bridging, and may also be a proxy for more complex mechanisms that protect organic matter, such as stabilization of soil aggregates by Ca^{2+}.[16] Regardless of the mechanism(s), these facts suggest that release of Ca from carbonate and silicate dissolution may link SOC storage to mineral weathering in Mollisols. This effect would be analogous to the link between silicate weathering and SOC

82 mediated by reactive iron and aluminum in other soil types.[20] The hypothesis that Ca inputs from
83 weathering enhance SOC in Mollisols is challenging to test because soil Ca availability depends
84 on complex interactions between vegetation, geology, and climate.

85 We addressed the role of Ca in Mollisol SOC storage by developing and applying a novel
86 geochemical model across the conterminous USA. Our modeling approach leveraged soil
87 mineralogy data[21] that enabled us to represent soil chemical processes at an unprecedented spatial
88 extent. We designed our model to track the inputs and outputs of major cations and anions to the
89 soil solution, simulating soil pH, mineral weathering rates, and associated Ca release and retention.
90 We estimated the effect of Ca availability on SOC statistically while accounting for vegetation,
91 climate and other confounding factors. Next, we used the model to constrain specific Ca sources:
92 carbonate weathering, silicate weathering, and atmospheric deposition. We then quantified the
93 sensitivity of SOC storage to Ca inputs from weathering in Mollisols (Figure 1a) versus non-
94 Mollisol soils. Using this approach, we were able to test the hypothesis that Ca released from
95 carbonate and silicate weathering helps to explain the C richness of Mollisols.

96 **Geochemical model performance**

97 We used our geochemical model to estimate Ca availability in soil across the conterminous USA.
98 We first parametrized the model with input data including climate, atmospheric deposition of major
99 solutes, net primary productivity, agricultural element budgets, and soil mineralogy (see Methods).
100 The model integrated these variables by linking inputs and outputs of solutes, the release of CO_2
101 and organic acids by biota, and mineral weathering via a set of pH-dependent equilibrium
102 reactions. We calibrated two unconstrained parameters related to mineral surface reactivity,
103 training the model to match modern observations of soil pH. The model was able to explain 69%
104 of the spatial variation in depth-averaged soil pH (0-100 cm) across the USA. Performance was

105 more modest when predicting soil exchangeable cations: the model explained 40% of the variation
106 in the soil exchangeable Ca^{2+} fraction and 66% of the variation across all exchangeable cations
107 when applied to validation data (Figure S1, Figure S2, Table S1). Notably, these validation results
108 were depth-averaged to 100 cm because our model treated the uppermost 100 cm of soil as
109 chemically and mineralogically homogenous. A vertically resolved, multi-phase reactive transport
110 model would better capture gradients in soil pH, weathering rates, and exchangeable ions, but at
111 the cost of added complexity and uncertain parameters (e.g., rates of biological nutrient uplift). We
112 expect that the geographic patterns captured by our simplified geochemical model would likely be
113 qualitatively similar if vertical resolution was added because these patterns are driven by
114 continental-scale gradients in soil soil pH, which are stronger than vertical gradients.[22]

115 **Relating Ca to SOC stocks**

116 After calibrating the geochemical model, we developed a statistical approach to link soil Ca with
117 SOC stocks. Mollisols are characterized by thick, C-rich A-horizons;[14] hence we used total A-
118 horizon SOC—incorporating both topsoil thickness and C content—as an index that captures the
119 primary mode of C storage in Mollisols. We obtained SOC stock data from two databases: the US
120 Department of Agriculture Rapid Carbon Assessment and the National Cooperative Soil Survey
121 archives[23,24] (Figure 1b). We then quantified the relationship between A-horizon SOC stocks and
122 modeled soil exchangeable Ca^{2+} across the conterminous USA using multiple linear regression.
123 We included eight potentially confounding factors in the regression: (1) the pre-agricultural
124 grassland and savanna distribution, which we approximated with a potential vegetation map
125 derived from remotely sensed patches of relict vegetation;[25] (2) mean annual soil temperature; (3)
126 mean annual precipitation; (4) soil silt and clay content (5) soil drainage class; (6) soil pH derived
127 from the geochemical model; (7) net primary productivity, and (8) the sum of non-Ca^{2+}

exchangeable cations derived from the geochemical model (Mg^{2+}, K^{+}, Na^{+}, Al^{3+}, and H^{+}). We also experimented with including interaction terms between vegetation and geochemical parameters, but these were not statistically significant at a threshold of p=0.05, and so we did not include them. The regression model explained 30% of the variation in A-horizon SOC stocks. Comparison of the scaled regression coefficients revealed that net primary productivity and soil temperature were the most important predictors of A-horizon SOC storage, followed by exchangeable Ca^{2+}, the presence of grasslands or savannas, and then other factors (Figure 2; Table S3). These results indicate that modeled exchangeable Ca^{2+} is positively correlated with A-horizon SOC storage. The combined effect of other exchangeable ions on SOC across the USA—including the effect of Al^{3+} and H^{+} in acid soils—was weak. This implies that Ca, rather than total cation exchange capacity, drives this correlation.

Notably, the association between modeled soil Ca availability and SOC is subject to several sources of uncertainty. The geochemical model was relatively skilled at matching spatial patterns in soil pH, yet the majority of the variation in the soil exchangeable Ca^{2+} fraction remained unexplained and the relative abundances of individual non-Ca^{2+} base cations Mg^{2+}, K^{+}, and Na^{+} could not be predicted with confidence (Figure S2, Table S1). These uncertainties likely reduced effect sizes for both Ca^{2+} and non-Ca^{2+} base cations in the regression analysis due to statistical attenuation bias. In addition to this limitation, the majority (70%) of the variation in A-horizon SOC stocks remained unexplained by our regression, meaning that unobserved confounding factors could affect our results. Keeping these caveats in mind, our modeled results successfully recover the positive relationship between measured exchangeable Ca^{2+} and SOC that emerges in purely observational studies.[18,19] This suggests that simulated exchangeable Ca^{2+}, while highly

approximate, was an effective index for soil available Ca and its potential to facilitate organo-mineral association.

While our model-driven estimates of Ca^{2+} are uncertain, they enable us to test specific causal hypotheses that are not accessible using direct observations. For instance, statistical correlations between metal ions and SOC concentrations may emerge simply because organic matter provides more sorption sites for metals.[26] We were able to control for this effect by correcting for the contribution of soil organic matter to cation exchange capacity, and found that the positive association between simulated exchangeable Ca^{2+} and SOC is robust (Figure S3). More importantly, our modeling approach allowed us to consider how the ultimate drivers of Ca availability might affect SOC storage. Specifically, we were able to estimate indirect effects of carbonate and silicate weathering on SOC storage mediated by soil Ca availability.

Linking Ca sources to SOC storage

We evaluated the long-term effect of silicate and carbonate weathering on A-horizon SOC stocks by constructing counterfactual scenarios in which natural Ca sources were suppressed under preindustrial conditions. We focused on pre-industrial conditions to isolate the effects of geologic sources of Ca over the centennial timescales that govern SOC accrual. To represent preindustrial conditions, we re-parametrized the model to reflect atmospheric deposition in 1850[27] (see Methods), eliminated agricultural processes, and ran simulations under preindustrial carbon dioxide levels. We then performed the following steps: (1) we set carbonate weathering, all silicate weathering, or atmospheric Ca deposition to zero in the geochemical model, (2) we used updated outputs from the geochemical model to generate predictions using the previously fitted regression, and (3) we quantified changes in the predicted A-horizon SOC stocks. For reference, we also created a counterfactual scenario in which all vegetation was assumed to be non-grassland.

Our model experiment revealed that both carbonate and silicate weathering help to explain A-horizon SOC stocks across the USA. Across the Mollisol regions of the conterminous USA, predicted preindustrial A-horizon SOC storage was 6.5% (0.5 Pg C) lower when carbonate weathering was eliminated, 2.4% (0.2 Pg C) lower when silicate weathering was eliminated, and 16% (1.2 Pg C) lower when both were eliminated together. The effect of eliminating all weathering was similar to the effect of eliminating grassland vegetation, which reduced A-horizon SOC storage by 19% (1.5 Pg C) (Figure 3b). We obtained the same statistics for non-Mollisol soils and computed the difference in the sensitivity of Mollisol and non-Mollisols regions, i.e., the effect of eliminating each factor on Mollisols minus the effect on non-Mollisols. He found that A-horizon SOC stocks in Mollisols were particularly sensitive to Ca inputs from carbonate weathering and the combined action of carbonates and silicates (Figure 3b). Eliminating grassland vegetation also had a substantially larger effect on SOC in Mollisols (Figure 3b, gray square). These results suggest that the C richness of Mollisols is related to vegetation and are also consistent with our hypothesis that Ca inputs from mineral weathering augment SOC in Mollisols.

Interestingly, eliminating carbonate weathering had a modest effect on A-horizon SOC storage when considered alone, but a more substantial effect when silicate weathering was also eliminated. Similarly, eliminating Ca inputs from silicate weathering had no clear effect on A-horizon SOC storage on its own, but a substantial effect when both mineral sources were eliminated. This result emerged from the geochemical model because carbonate weathering and silicate weathering suppressed each other via their alkalizing effect on soil pH; hence eliminating one Ca source in the model yielded a compensatory increase in Ca release from the other. Suppression of silicate weathering by carbonate weathering has been observed in the field across soil chronosequences[28–30] and in weathering mesocosms,[31] which suggests that this model behavior

196 captures a real geochemical dynamic. When either silicates or carbonates are sufficiently abundant,
197 soil Ca availability is high and Ca^{2+} generally predominates over other exchangeable ions. These
198 conditions appear to favor Mollisol formation and SOC accrual across a range of geologic settings.

199 Our model suggests that the elevated Ca inputs associated with Mollisols in the
200 midcontinental USA are derived from specific geologic sources, particularly carbonate minerals
201 (Figure 3b). Glacial deposition explains elevated carbonate weathering in the north-central USA,
202 where lobes of the Laurentide ice sheet ground up and distributed underlying limestone and
203 dolomite rocks during the last ice age.[32] Farther south, soil carbonates are abundant in the aeolian
204 Bignell Loess deposits[33] and in the predominately limestone rocks of the Edwards Plateau,[34] both
205 of which support Mollisols. Carbonate minerals are also abundant in the arid Western USA;
206 however, our geochemical model predicts that carbonates are either a minor source or a Ca sink in
207 this region (Figure S3). While some of the carbonates in these soils may be derived from
208 sedimentary rocks, desert carbonates are often primarily derived from in-situ precipitation of
209 $CaCO_3$ from aeolian Ca.[35] Our model suggests that some of these carbonates may be slowly
210 weathering under late-Holocene conditions, supplying Ca to overlying Mollisols.

211 Our model also predicts that inputs of Ca from deposition are significant in much of the
212 USA (Figure 3c); however, we found that atmospheric deposition of Ca is a minor control on A-
213 horizon SOC storage (Figure 3a). We assumed that preindustrial Ca deposition was five-fold lower
214 in North America than at present based on paleo dust records.[36] Dust fluxes in the midcontinental
215 USA were substantially higher in the late Pleistocene than in recent preindustrial times due to
216 glaciation.[37] Ca in modern soil carbonates is often inherited from Pleistocene dust,[38] and
217 carbonates continue to weather in Pleistocene loess deposits. Thus, over geologic timescales,

atmospheric Ca deposition during glacial periods may set the stage for future carbonate weathering, potentially helping to build Mollisol SOC stocks.

Our analysis finds a role for Ca in Mollisol SOC storage but also suggests that grassland and savanna vegetation promote SOC in Mollisols independent of other factors. Grasslands and savannas can be maintained by fire, helping grasses to persist in climates that would otherwise support forest.[39,40] In this case, fire regimes that maintain grass dominance might directly determine where Mollisols form.[9] On the other hand, Mollisols are notably uncommon in tropical grasslands and savannas,[41] which suggests that ecological factors common to grasslands and savannas—including high belowground productivity and fire—are not sufficient to generate the C-rich A horizons characteristic of Mollisols. Tropical soils are typically highly weathered, host less reactive minerals, and are generally more acidic than temperate soils that received Ca-rich minerals following Pleistocene glaciation.[22,42] These geologic limits to Ca supply, in addition to climate, may curtail Mollisol development in the tropics. By contrast, multiple overlapping environmental factors—including Ca weathering in post-glacial soils, cooler temperatures, mesic climate, and the presence of grasses—converge in certain temperate regions, and Mollisols are an emergent result of these overlapping factors.

Implications for Mollisol conservation and climate mitigation

Our results imply that changes in soil Ca inputs due to cultivation might affect SOC cycling in Mollisols. To address this possibility, we used our model to evaluate the magnitude of changes to the Ca balance of Mollisol croplands relative to preindustrial conditions. We parametrized the model with modern day atmospheric deposition chemistry, enabled agricultural fertilizer addition and nutrient removal, and estimated agricultural liming rates. This analysis shows that soil Ca cycling has changed dramatically in two ways (Figure 4). First, the model predicts that acid inputs

from fertilizer and atmospheric deposition have accelerated Ca release from carbonate weathering by 20% in Mollisols. Second, agricultural liming has massively increased Ca inputs to cropland soils (Figure 4). Taking modeled liming rates as a reference point, agriculture has increased Ca inputs to Mollisol cropland soils by approximately 5-fold and increased Ca input to non-Mollisol cropland soils by 10-fold relative to preindustrial levels. Alternatively, we can take the most recent available agricultural census liming data,[43] which are from 1987, as a reference point. We estimate that agriculture has increased Ca inputs to Mollisol cropland soils by 6-fold and non-Mollisol cropland soils by 19-fold based on 1987 liming rates assuming that lime is 20% dolomite and 80% calcite.[44]

Clearly humans have dramatically altered the Ca cycle, and this has the potential to affect SOC storage in Mollisols. The finding that agriculture has accelerated dissolution of native carbonates is consistent with other studies that have linked agricultural soil acidification to soil inorganic C loss, although the acceleration of carbonate weathering predicted by our model is modest compared to estimates in highly acidified systems (e.g., in China).[45–47] Our simulations indicate that the more significant perturbation to the soil Ca cycle is agricultural lime addition. Adoption of enhanced silicate[48] or carbonate[49] weathering for carbon dioxide removal will further perturb the Ca cycle. These practices increase soil Ca inputs, which our analysis suggests contribute to SOC storage over geologic timescales. However, increased Ca inputs have occurred in response to unprecedented acid addition to cropland soils, and the effects of these competing processes are hard to predict. For instance, field experiments indicate that the effect of agricultural liming on SOC is highly variable over the short term.[50] Similarly, enhanced silicate weathering does not necessarily benefit SOC storage in the short term,[51,52] although a compilation of experiments suggests a positive effect on average.[53] Liming may affect SOC differently than

natural weathering because it is intermittent: in the USA only 5-20% of cropland is limed in any given year.[54] Variable Ca availability caused by intermittent liming may alternately stimulate and suppress decomposition, with net effects that are challenging to predict.

In the broader context of conservation agriculture, our results suggest that farming practices that mimic pre-agricultural vegetation in grasslands by increasing root inputs, increasing plant diversity, or reducing tillage may not be sufficient to preserve Mollisol SOC. Instead, vegetation-focused strategies may need to be complemented with geochemical strategies that mimic the natural Ca cycle of these soils. For instance, reducing excess N can protect soil carbonates, which reduces emissions from dissolution of soil inorganic C by strong acids,[47] while also preserving a critical Ca reservoir that likely helps to protect SOC. In addition, changing the cadence and quantity of lime applied to croplands could better simulate the natural weathering regime. These efforts must be supported by collection of baseline statistics on the agricultural Ca budget, which remains poorly quantified.[54] Closing these knowledge gaps is critical to managing Earth's most fertile soils sustainably.

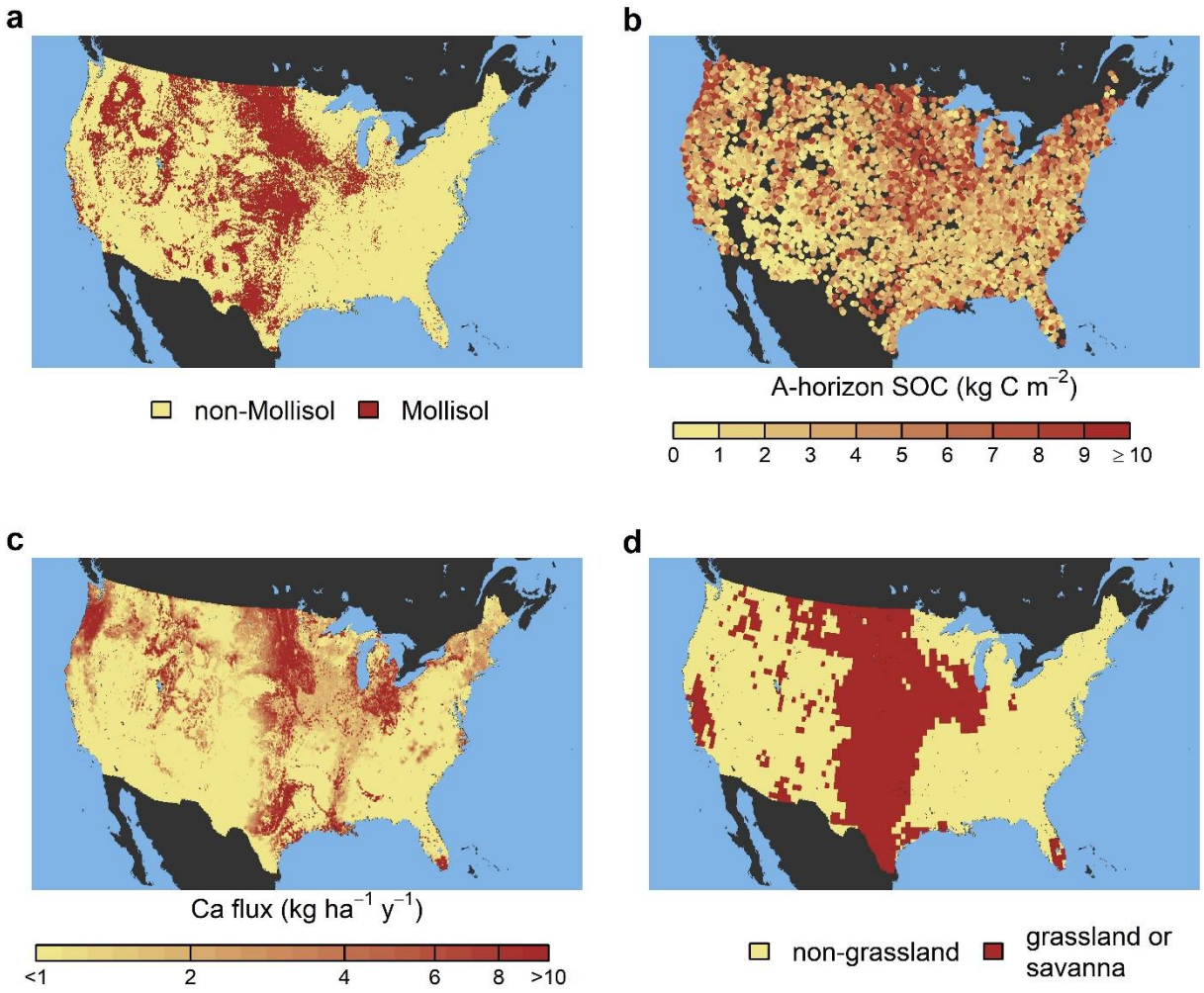

278

279 **Figure 1. Potential environmental controls on Mollisols across the USA.** (a) The distribution
280 of the Mollisol soil order across the conterminous USA based on digital soil mapping.[55] (b) Point
281 observations of A-horizon soil organic carbon (SOC) derived from two databases.[23,24] (c)
282 Modeled preindustrial available calcium flux from silicate weathering, carbonate weathering, and
283 atmospheric deposition. (d) The potential distribution of grasslands and savannas.[25]

284

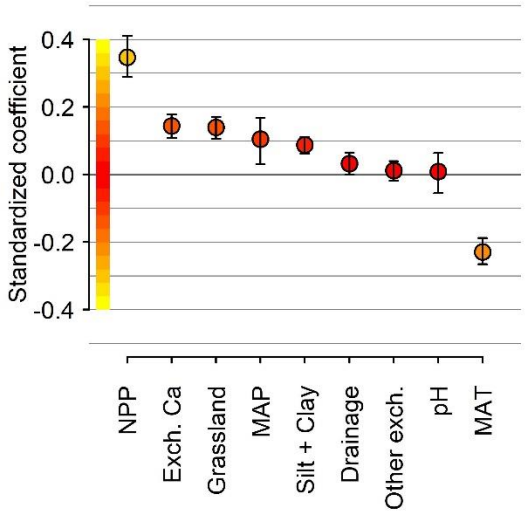

285

286 **Figure 2. Predictors of A-horizon SOC stocks across the USA.** Standardized regression
287 coefficients are derived from a multivariate linear regression model. Whiskers show 95%
288 confidence intervals derived from a spatial blocked bootstrapping procedure (see Methods).
289 Standardization was performed by dividing each non-binary variable by two times the standard
290 deviation.[56] The absolute value of each regression coefficient is an index of how strongly related
291 each variable is to A-horizon SOC stocks. Abbreviations: NPP = net primary productivity, Exch.
292 Ca = total exchangeable Ca^{2+}, MAP = mean annual precipitation, Other exch. = sum of non-Ca
293 exchangeable ions, MAT = mean annual soil temperature.

294

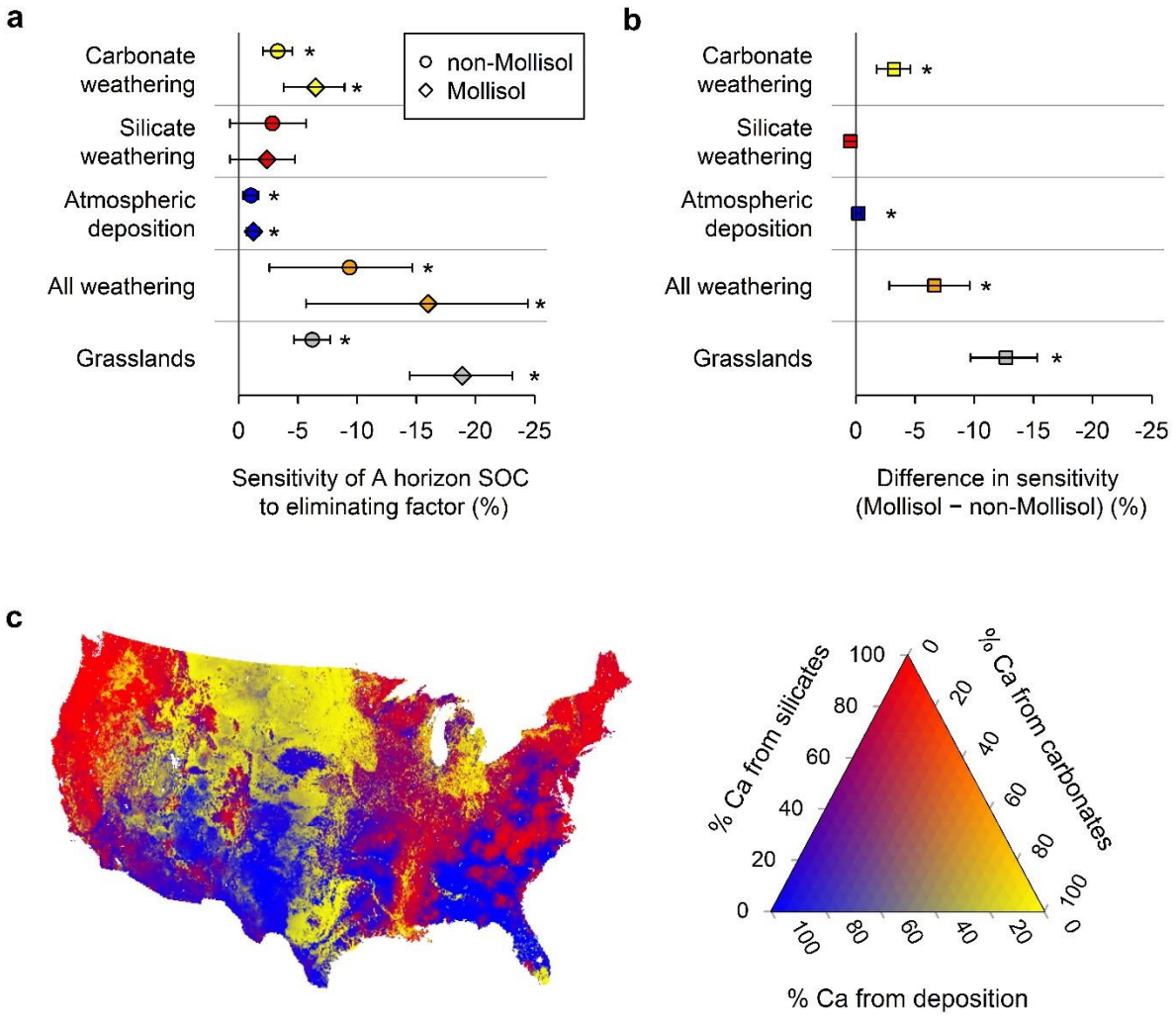

295

296 **Figure 3. Sensitivity of Mollisol extent and A-horizon organic carbon to Ca sources**. (a) The
297 relative effect of removing Ca sources on predicted A-horizon soil organic carbon (SOC) stocks
298 across non-Mollisol soils (circles) versus Mollisols (diamonds). Sources include carbonate
299 weathering (yellow), silicate weathering (red), atmospheric deposition (blue), and carbonate and
300 silicate weathering combined (orange). The effect of setting all grassland vegetation to non-
301 grassland is shown in gray. (b) The difference in sensitivities: effect of removing factor in
302 Mollisols minus effect in non-Mollisols. Whiskers show 95% confidence intervals derived from
303 spatial blocked bootstrapping (see Methods) and are marked with an asterisk when they do not
304 overlap zero. (c) The relative contributions of carbonate weathering, silicate weathering, and
305 atmospheric deposition to available Ca across the USA.

306

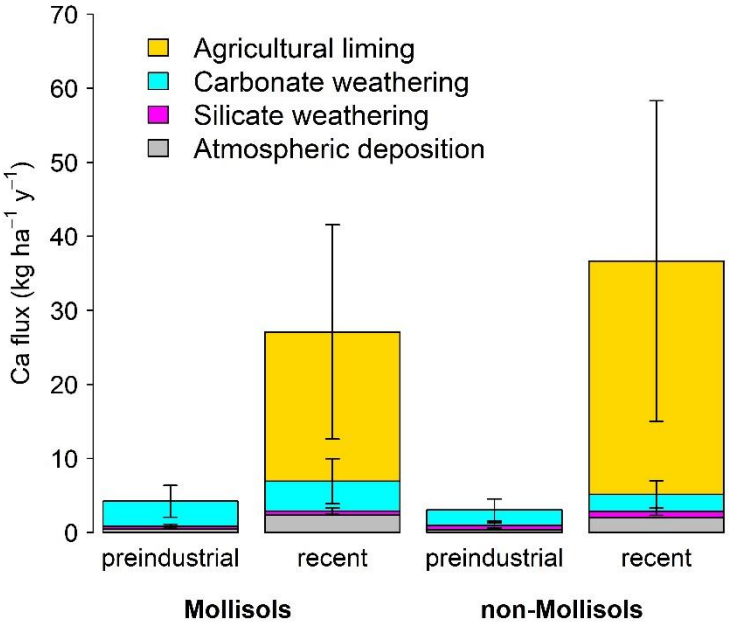

307

308 **Figure 4. Modeled Ca fluxes to croplands, preindustrial (1850) versus recent (2000-2010).**
309 Stacked bars show the Ca sources: atmospheric deposition, carbonate weathering, silicate
310 weathering, and agricultural liming. Data for Mollisol regions are shown on the left and non-
311 Mollisol regions on the right. Whiskers show Monte Carlo standard errors derived from
312 approximated parameter uncertainties. Liming estimates are based on the conservative
313 assumption that farmers lime sufficiently to maintain soil pH (see Supplementary Information).

314

Methods

Quantifying global role of Mollisols

We calculated the total land area of Mollisols, the fraction of global agricultural production occurring on Mollisols, and the fraction of agricultural SOC stored by Mollisols using the Harmonized World Soil Database, Version 2.0 (HWSD).[2] For this analysis we assumed that the distribution of Mollisols can be approximated by aggregating three World Reference Base soil groups: Chernozems, Phaeozems, and Kastanozems.[57] HWSD soil mapping units were assigned as Mollisol or non-Mollisol based on the dominant soil type in each unit. SOC was calculated from the HWSD and summed to 1 m depth. We then combined the HWSD with the 1 km resolution GFSAD 2010 croplands mask[3] to estimate the area of croplands and cropland SOC storage. Production of wheat, corn, and soy occurring on Mollisols was obtained by combining the HWSD with SPAM global production maps for 2010.[58] Production values were rescaled to calories based on UN Food and Agriculture Organization Annex I food composition tables.[59]

Geochemical model overview

We developed a simplified geochemical model to simulate the release of Ca from silicate and carbonate weathering in the top 1 m of soil across the USA. We parametrized the model with existing data when possible and then calibrated unknown parameters related to mineral surface reactivity so that modeled soil pH matched observed modern soil pH across the study region. We based our model on existing geochemical models that were designed to simulate soil acid-base chemistry in response to acid rain.[60] Our model also incidentally resembles approaches used to simulate enhanced silicate weathering,[61] although it was not designed for this purpose and is less complex. The model treated the entire upper 100 cm of soil as a single chemically homogeneous reservoir, tracking the inputs and outputs of seven ions that control soil pH and weathering rates: Ca^{2+}, Mg^{2+}, Na^{+}, K^{+}, SO_4^{2-}, NO_3^{-}, Cl^{-}. These ions were sourced from dissolution of silicate and

carbonate minerals, atmospheric deposition, agricultural inputs, and biological fixation in the case of N. Ions were lost via leaching, carbonate mineral precipitation, export in crop biomass, and volatilization in the case of N. Additional ions were assumed to equilibrate instantaneously with the soil solution and hence were modeled implicitly as a function of other factors: H^+, Al^{3+}, $Al(OH)^{2+}$, $Al(OH)_2^+$, AlH_2Org^{2+}, $AlHOrg^+$, OH^-, CO_3^-, HCO_3^-, H_2Org^-, $HOrg^{2-}$, Org^{3-}, and $Al(OH)_4^-$. We approximated ion activities with concentrations because, under most conditions, modeled ionic strengths were too low to affect our results. Mineral concentrations were treated as constant at the timescales being modeled. While the model was able to simulate year-to-year weathering dynamics, for the purposes of this analysis, we applied a steady-state solution because this simplified computations substantially. The model had nine governing equations: one for each of the seven conserved ions and two algebraic constraints stipulating charge balance and conservation of ions adsorbed on the soil exchange complex (Table S4). A full description of the model is provided in the Supplementary Information file.

Input data

Whenever possible, we used spatially explicit environmental data to assign model parameters. When time series were available, we used time-averaged environmental parameters to drive the model, setting the years 2001-2010 as our reference period for recent environmental conditions. To capture pre-industrial conditions, we reset deposition rates for N and S, reset atmospheric pCO_2, and turned off the model's agricultural nutrient budget.

To parametrize climate and soil hydrologic properties, we used several sources. We derived soil temperature from statistical estimates of the mean annual soil temperature at 50-15 cm depth,[62] which we assume approximates the mean temperature of the upper 100 cm of soil on an annually averaged basis. We calculated recharge (RC) using the Global Streamflow

Characteristics Database (GSCD), which provides 0.125 degree resolution estimates of streamflow and base flow index.[63] We calculated recharge by multiplying streamflow by the baseflow index. We constrained soil moisture with the satellite-informed Global Land Evaporation Amsterdam Model (GLEAM) V3.8 root zone soil moisture dataset (0.25 degree resolution).[64] We also obtained pedotransfer-based maps of wilting point and field capacity associated with GLEAM. Finally, we parametrized net primary productivity (NPP) using MOD17 (500 m resolution).[65]

We parametrized soil mineralogy using two sources. For silicate minerals, we spatially interpolated data from the North American Soil Geochemical Landscapes Project (NASGLP),[21] which includes estimates of major element abundance and quantitative X-ray diffraction data for a selection of silicate and carbonate minerals. We used these data to directly constrain some minerals and approximate concentrations of others that are not directly reported by NASGLP. First, we averaged A-horizon and C-horizon data at the NASGLP sampling locations. We then interpolated the NASGLP data for each mineral to locations where we ran the geochemical model, using inverse distance weighting with an exponent of 2 and an averaging neighborhood of 75 km. Plagioclase feldspar and the plagioclase anorthite fraction (fAn) were estimated by first multiplying the molar concentration of Na from the NASGLP by the formula weight of albite. Where albite exceeded 80% of the total plagioclase feldspar content obtained from the NASGLP, albite was reset to 80% of the plagioclase content. Anorthite was then assumed to make up the remainder of the plagioclase pool.[20] K-feldspar, hornblende, and pyroxene were taken directly from the NASGLP X-ray diffraction estimates. To represent clay minerals, we limited our analysis to chlorite (clinochlore) and illite (approximated as muscovite), which we treated as generalized categories that stand in for the full diversity of Mg- and K-bearing 2:1

385 phyllosilicates (e.g. vermiculite and smectite group clays). Illite was calculated by subtracting
386 the K in K-feldspar from total K and assigning all residual K to illite. Similarly, chlorite was
387 calculated by first calculating the amount of Mg in hornblende, pyroxene, and dolomite (Table
388 S5). This value was subtracted from total Mg, and any residual Mg was assigned to chlorite.

389 To estimate carbonate mineral stocks, we did not use NASGLP data directly. Given the
390 high weatherability of carbonates, small quantities of carbonate mineral had a large effect on
391 modeled soil pH values; hence we used high-resolution digital soil maps from NATSGO[55] to
392 ensure accurate assignment of soil carbonate content. We first calculated the stock of carbonate
393 in $CaCO_3$ equivalents to 1 meter depth from NATSGO. Next, we subdivided this stock into
394 calcite and dolomite components by using the data from the NASGLP to calculate the ratio of
395 calcite to dolomite. In addition to $CaCO_3$ content, we derived soil texture (silt, sand, and clay
396 percentages), cation exchange capacity, and soil bulk density parameters from NATSGO,
397 averaging these properties over the top 1 meter of soil or to bedrock if shallower than 1 meter.
398 All NATSGO soil properties were summarized by calculating the share-weighted average within
399 soil mapping units. Data were then extracted using the 30-meter resolution gridded version of
400 NATSGO.

401 We parametrized the cropland N inputs and outputs using a county-level nutrient budget
402 for the period 1987-2012.[66] We ran the geochemical model in one of two modes, either with
403 cropland nutrient imports and exports enabled or with only natural N fixation rates enabled. We
404 determine which mode to use by assigned modeled locations to cropland or non-cropland land
405 cover using the GFSAD 1 km cropland mask.[3]

406 We parameterized deposition of N, S, Cl, Ca, Mg, Na, and K, using gridded data from the
407 US Environmental Protection Agency's National Trend Network,[67] which we averaged for 2001-

2010. To represent preindustrial deposition of N and S, we used the multi-model average from the ACCMIP project for the year 1850.[27] For Cl, Ca, Mg, Na, and K no data from before the year 2000 were available. Human activity has increased deposition of base cations, including Ca, in the Western USA.[36] To account for this trend, we applied a factor of 5 difference between recent and preindustrial times, which approximates dynamics recorded in lake sediment cores in Colorado.[36] We applied this multiplier to Ca, Mg, and K, but left Na unchanged since this solute is primarily derived from marine aerosols outside of deserts.

Model calibration and uncertainty

We implemented the model at point locations, extracting data from the aforementioned environmental datasets at each point. For the calibration and validation steps, we selected points by acquiring soil pH data from the USDA NRCS National Cooperative Soil Survey (NCSS) Kellogg Soil Survey Laboratory database. We computed depth weighted average pH values in a 1:1 water matrix for all soil profiles with available data to a depth of 1 m, or to the depth of the lowermost C horizon in cases where the profile terminated below 1 m. Similarly, we computed depth-weighted average values for exchangeable cations using the NCSS database. We represented Ca^{2+}, Mg^{2+}, Na^{+}, and K^{+} using NH_4-acetate (pH 7) extraction data and Al^{3+} from KCl extraction. Exchangeable H^{+} was estimated by subtracting the sum of exchangeable Ca^{2+}, Mg^{2+}, Na^{+}, K^{+}, and Al^{3+} from the cation exchange capacity (CEC) obtained by the NH_4-acetate method. When the sum of these ions exceeded the CEC, exchangeable H^{+} was set to zero and the values of all ions were rescaled by the value (CEC / sum cations) so that the sum equaled the CEC.

We spatially resampled the pH and exchangeable cation data by binning them into 1 degree by 1 degree cells based on their latitude and longitude and then resampling 6,000 locations with replacement, with sampling weights inversely proportional to the number of

profiles in each cell. We extracted environmental data at these points and discarded those with missing data, yielding 4,149 unique pH observations that were evenly distributed across the conterminous USA (Figure S1). Exchangeable ions were only reported at 2,484 locations with pH measurements. Because we resampled with replacement, some soil profiles occurred more than once by design; the total number of pH observations was 5,389 (including pseudo-replicates) and the total number of exchangeable cation observations was 3,280.

We calibrated the model by randomly sampling 2,000 pH training points from the NCSS profiles and using them for model inversion based on soil pH. We optimized two parameters, r_2 and r_3, which controlled the reactivity for secondary phyllosilicate minerals and carbonate minerals respectively (see Supplementary Information). We calibrated the model using a Markov Chain Monte Carlo (MCMC) approach, applying the adaptive Metropolis Hastings algorithm with delayed rejection[68] implemented via the R package FME.[69] The cost function was defined to minimize the sum of squared errors in soil pH. We initiated the MCMC algorithm with manually calibrated initial parameter values and uninformative priors. The initial model variance was set equal to the mean squared residuals based on the initial parameter estimates, and the initial jump values were set to 10% of the initial parameters. The adaptive stage of the algorithm was run for a burn-in period of 1,000 iterations updating the covariance matrix every 50 iterations with the number of delayed rejections steps set to 2. After burn-in sampling continued for an additional 1,000 iterations. We checked for convergence by running the algorithm using perturbed values of the starting parameters and different training samples and found that results were comparable. The final calibration yielded values of $10^{-6.7}$ for r_2 and $10^{-6.4}$ for r_3.

We estimated uncertainty in modeled Ca fluxes using a Monte Carlo approach. Parameter uncertainties were largely unconstrained and could only be approximated. Given this, our goal

was to quantify the robustness of our results given arbitrary but substantial parameter uncertainty. Based on our best judgement, we divided the model parameters into “low”, “moderate” and “high” uncertainty categories. Low uncertainty parameters were treated as fixed. Moderate uncertainty parameters were randomly perturbed within a uniform range spanning 50% - 150% of the default value. High uncertainty parameters were varied uniformly within an order or magnitude range: each was transformed with a base-10 logarithm, randomly perturbed within a range spanning 50% - 150%, and then transformed back to the original scale. This procedure was repeated 1,500 times at the model calibration locations. We treated the coefficient of variation of the average Ca fluxes derived from this process as an approximate estimate of uncertainty. Parameters assigned moderate uncertainty included: all mineral surface areas, combined N inputs, N removal in croplands, dissolved organic carbon inputs, the charge density, C:N ratio, and temperature dependence (Q_{10}) of dissolved organic matter, the leaching rate, and both the temperature dependence and H^+ reaction order for silicate weathering. Parameters assigned high uncertainty included, the decomposition rate coefficient for dissolved organic matter, the N volatilization rate, weathering rate coefficients for silicates and carbonates (r_1, r_2, and r_3), all equilibrium constants relating to dissolved organic matter, and all ion exchange selectivity coefficients.

Statistical analysis

After calibrating the geochemical model, quantified the strength of the relationship between soil Ca availability and A-horizon SOC using multiple linear regression. We obtained A-horizon SOC stocks from the RaCA[23] and the NCSS[24] databases. We ran regressions on the full population of 11,332 A-horizon SOC estimates from RaCA and NCSS. When working with data from RaCA and NCSS, we calculated the SOC stock in all horizons with the master designation “A”. The

SOC stock (kg C m^{-2}) was calculated from the total carbon percentage (C%), the inorganic carbon percentage (IC%), A-horizon thickness (TH, cm), rock fraction (RF, unitless) and bulk density (BD, g cm^{-3}) as:

$$SOCstock = ((C\% - IC\%)/100)*BD*TH*(1-RF)*10 \quad \text{(Equation 23)}$$

Inorganic carbon was calculated from $CaCO_3$ equivalents reported in RaCA. In the cases where IC% exceeded C%, OC% was set to zero. In the case of NCSS, we used the "estimated organic C" field, which is corrected for IC where applicable, or organic carbon content estimated via the Walkley Black method when this field was not available. After calculating SOC in each A horizon, we summed all A horizon stocks for each pedon to obtain total A-horizon SOC. We log transformed A-horizon SOC stocks before fitting the model.

We used linear regression to model log-transformed A-horizon SOC as a function of total exchangeable Ca^{2+} (ceq kg^{-1}) and other ecologically important or potentially confounding factors. In addition to exchangeable Ca^{2+}, we included two additional outputs of the geochemical model: the sum of non-Ca^{2+} exchangeable cations and the simulated soil pH. We used potential natural vegetation maps[25] to capture the effect of grasses, treating grass presence as a binary predictor with grasslands and savannas combined into a single category (present = 1, absent = 0). We accounted for the effect of plant inputs on SOC by including the logarithm of average NPP, derived from MOD17 for the period 2001-2010. We used gridded climate maps to control for mean annual soil temperature[62] and mean annual precipitation (1991-2020).[70] We also controlled for the average silt plus clay content of the top meter of soil and soil drainage class, which we derived from NATSGO.[55] Drainage class categories were assigned numerical values from 1-7, with 1 being excessively drained and 7 being very poorly drained. We compared the relative importance of different predictors in the regression models by standardizing all predictors

upstream of fitting the models. We standardized by dividing continuous predictors by two times the standard deviation, which is recommended in cases when some predictors are binary.[56] We estimated uncertainty associated with the coefficients by performing nonparametric spatially blocked bootstrapping to account for spatial dependence.[20] This involved dividing the data into blocks defined by 2-by-2 degree grid cells and then resampling the cells with replacement 1,000 times. We fit a regression to each of the 1,000 resampled datasets and stored the regression coefficients. We then calculated bias corrected and accelerated 95% confidence intervals from the bootstrap replicates.[71]

After fitting the regression, we estimated the sensitivity of A-horizon SOC to eliminating specific Ca sources under preindustrial conditions. This first involved using the geochemical model to estimate soil exchangeable Ca^{2+} under a preindustrial baseline scenario. In the baseline scenario, we eliminated all agricultural components of the geochemical model and used our best estimate of preindustrial deposition rates for major cations and anions (see Supplemental Text). Next, we evaluated the sensitivity to cation inputs from carbonate weathering and silicate weathering by running the model with each mineral cation source eliminated, setting either carbonate or silicate surface areas to zero. This meant that Ca, but also Mg, K, and Na weathering fluxes were affected by removing each source. To evaluate sensitivity to deposition, we set all base cation deposition fluxes to zero. Each of these modified model runs generated predictions of exchangeable Ca^{2+} in the absence of each cation source. We also quantified the effect of eliminating grasslands by setting the grassland predictor to zero everywhere.

To calculate sensitivity values, we followed the following protocol. First, we fit a linear regression to the SOC data using present day model outputs as described above, but with response and predictors left unscaled. Next, we used the fitted regression to obtain predictions in

523 a 10-km grid across the USA with inputs derived from each of the preindustrial scenarios
524 described above. We then calculated the total stock of A-horizon SOC in Mollisols and non-
525 Mollisol soils across the grid under the baseline scenario. The distribution of Mollisols was
526 obtained from NATSGO, and 10-km grid cells were assigned to the Mollisol category when
527 Mollisols comprised the dominant soil order at the coordinates of the grid cell center. Within
528 each soil taxonomic domain, we estimated the sensitivity to eliminating Ca sources and
529 grasslands as the percent change in SOC from the preindustrial baseline after each factor was
530 eliminated: 100*[(SOC under elimination scenario – SOC under baseline scenario) / SOC under
531 baseline scenario]. We estimated uncertainty in the sensitivity values by repeating this protocol
532 1,000 times during the spatially-blocked bootstrap resampling and calculating bias-corrected
533 95% confidence intervals as above. We also calculated the difference in sensitivity in Mollisol
534 versus non-Mollisol soils, estimating uncertainty using the same bootstrapping procedure.

535 Soil organic matter can contribute to cation exchange capacity, which may explain a
536 relationship between total exchangeable Ca^{2+} and SOC even in the absence of an effect of Ca on
537 SOC persistence. To account for this possibility, we conducted an additional regression analysis
538 after correcting total cation exchange capacity for the contribution of soil organic matter.
539 Corrected cation exchange capacity (CEC-c, ceq kg^{-1}) was obtained from the uncorrected CEC
540 and the soil organic matter percentage (SOM%) from NATSGO:

541 $$CEC\text{-}c = CEC - CEC\text{-}OM*(SOM\%/100) \quad \text{(Equation 24)}$$

542 Where CEC-OM is the cation exchange capacity of organic matter, assumed equal to 200 ceq kg^{-1}
543 .[72] This formula could generate negative or zero values, and so in cases where CEC-c was less
544 than a minimum value of 0.01 we re-set it to this value. The results of the regressions computed
545 with CEC-c were similar to the primary results (Figure S3).

Acknowledgements

Work at LLNL and UCD was primarily supported by Laboratory Directed Research and Development grant 22-ERD-19 under the auspices of the DOE, Contract DE-AC52-07NA27344. Additional support for manuscript preparation was provided by the LLNL Lab Directed Research and Development program (#24-SI-002), the DOE Office of Science 'Terraforming Soil' Carbon Negative Energy Earthshot Research Center (SCW1841). We thank Oliver Chadwick for feedback on early drafts of this manuscript and Claire Kouba and Iris Holzer for advice related to model development.

Author contributions: Conceptualization: EWS, HRG, RL, KJM, JPR, NS, DZ, KG; Methodology: EWS, KG; Investigation: EWS; Visualization: EWS; Supervision: EWS, KG; Writing—original draft: EWS; Writing—review & editing: EWS, HRG, RL, KJM, JPR, NS, DZ, KG

Competing interests: Authors declare that they have no competing interests.

Data and code availability: Model code and outputs are available at zenodo.org: https://doi.org/10.5281/zenodo.20671658.

References

1. Liu, X. *et al.* Overview of Mollisols in the world: Distribution, land use and management. *Can. J. Soil. Sci.* **92**, 383–402 (2012).
2. *Harmonized World Soil Database Version 2.0*. (FAO; International Institute for Applied Systems Analysis (IIASA);, 2023). doi:10.4060/cc3823en.
3. Teluguntla, P. *et al.* NASA Making Earth System Data Records for Use in Research Environments (MEaSUREs) Global Food Security Support Analysis Data (GFSAD) Crop

Mask 2010 Global 1 km V001. NASA Land Processes Distributed Active Archive Center https://doi.org/10.5067/MEASURES/GFSAD/GFSAD1KCM.001 (2016).

4. Thaler, E. A., Larsen, I. J. & Yu, Q. The extent of soil loss across the US Corn Belt. *Proc. Natl. Acad. Sci. U.S.A.* **118**, e1922375118 (2021).

5. Boincean, B. & Dent, D. Potential of Chernozem to Increase Food Security and Mitigate Global Warming. in *Farming the Black Earth* 189–204 (Springer International Publishing, Cham, 2019). doi:10.1007/978-3-030-22533-9_8.

6. Dokuchaev, V. V. *The Russian Chernozem*. (1883).

7. Rasse, D. P., Rumpel, C. & Dignac, M.-F. Is soil carbon mostly root carbon? Mechanisms for a specific stabilisation. *Plant Soil* **269**, 341–356 (2005).

8. Sokol, N. W., Kuebbing, Sara. E., Karlsen-Ayala, E. & Bradford, M. A. Evidence for the primacy of living root inputs, not root or shoot litter, in forming soil organic carbon. *New Phytol* **221**, 233–246 (2019).

9. Schmidt, M. W. I., Skjemstad, J. O. & Jäger, C. Carbon isotope geochemistry and nanomorphology of soil black carbon: Black chernozemic soils in central Europe originate from ancient biomass burning. *Global Biogeochemical Cycles* **16**, (2002).

10. Dreibrodt, S. *et al.* Earthworms, Darwin and prehistoric agriculture-Chernozem genesis reconsidered. *Geoderma* **409**, 115607 (2022).

11. Lynch, J. P. & Wojciechowski, T. Opportunities and challenges in the subsoil: pathways to deeper rooted crops. *Journal of Experimental Botany* **66**, 2199–2210 (2015).

12. Sprunger, C. D., Oates, L. G., Jackson, R. D. & Robertson, G. P. Plant community composition influences fine root production and biomass allocation in perennial bioenergy cropping systems of the upper Midwest, USA. *Biomass and Bioenergy* **105**, 248–258 (2017).

13. Smith, P. Soil carbon sequestration and biochar as negative emission technologies. *Glob Change Biol* **22**, 1315–1324 (2016).
14. Bockheim, J. G. Mollic Epipedon. in *Soil Geography of the USA* 29–46 (Springer International Publishing, Cham, 2014). doi:10.1007/978-3-319-06668-4_5.
15. Shabtai, I. A. *et al.* Calcium promotes persistent soil organic matter by altering microbial transformation of plant litter. *Nat Commun* **14**, 6609 (2023).
16. Rowley, M. C., Grand, S. & Verrecchia, É. P. Calcium-mediated stabilisation of soil organic carbon. *Biogeochemistry* **137**, 27–49 (2018).
17. Rowley, M. C., Grand, S., Spangenberg, J. E. & Verrecchia, E. P. Evidence linking calcium to increased organo-mineral association in soils. *Biogeochemistry* **153**, 223–241 (2021).
18. Rasmussen, C. *et al.* Beyond clay: towards an improved set of variables for predicting soil organic matter content. *Biogeochemistry* **137**, 297–306 (2018).
19. von Fromm, S. F. *et al. Continental-Scale Controls on Soil Organic Carbon across Sub-Saharan Africa*. https://soil.copernicus.org/preprints/soil-2020-69/ (2020) doi:10.5194/soil-2020-69.
20. Slessarev, E. W., Chadwick, O. A., Sokol, N. W., Nuccio, E. E. & Pett-Ridge, J. Rock weathering controls the potential for soil carbon storage at a continental scale. *Biogeochemistry* **157**, 1–13 (2022).
21. Smith, D. B. & Cannon, W. F. Geochemical and Mineralogical Data for Soils of the Conterminous United States.
22. Slessarev, E. W. *et al.* Water balance creates a threshold in soil pH at the global scale. *Nature* **540**, 567–569 (2016).

23. Wills, S. *et al.* Overview of the U.S. Rapid Carbon Assessment Project: Sampling Design, Initial Summary and Uncertainty Estimates. in *Soil Carbon* (eds Hartemink, A. E. & McSweeney, K.) 95–104 (Springer International Publishing, Cham, 2014). doi:10.1007/978-3-319-04084-4_10.
24. National Cooperative Soil Survey. National Cooperative Soil Survey Soil Characterization Database. (2018).
25. Ramankutty, N. & Foley, J. A. ISLSCP II Potential Natural Vegetation Cover. 1.72082 MB Preprint at https://doi.org/10.3334/ORNLDAAC/961 (2010).
26. Hall, S. J. & Thompson, A. What do relationships between extractable metals and soil organic carbon concentrations mean? *Soil Science Soc of Amer J* **86**, 195–208 (2022).
27. Lamarque, J.-F. *et al.* Multi-model mean nitrogen and sulfur deposition from the Atmospheric Chemistry and Climate Model Intercomparison Project (ACCMIP): evaluation of historical and projected future changes. *Atmos. Chem. Phys.* **13**, 7997–8018 (2013).
28. Anderson, S. P., Drever, J. I., Frost, C. D. & Holden, P. Chemical weathering in the foreland of a retreating glacier. *Geochimica et Cosmochimica Acta* **64**, 1173–1189 (2000).
29. Jacobson, A. D., Blum, J. D., Chamberlain, C. P., Poage, M. A. & Sloan, V. F. Ca/Sr and Sr isotope systematics of a Himalayan glacial chronosequence: carbonate versus silicate weathering rates as a function of landscape surface age. *Geochimica et Cosmochimica Acta* **66**, 13–27 (2002).
30. De Tombeur, F., Turner, B. L., Laliberté, E., Lambers, H. & Cornelis, J.-T. Silicon Dynamics During 2 Million Years of Soil Development in a Coastal Dune Chronosequence Under a Mediterranean Climate. *Ecosystems* **23**, 1614–1630 (2020).

31. White, A. F., Bullen, T. D., Vivit, D. V., Schulz, M. S. & Clow, D. W. The role of disseminated calcite in the chemical weathering of granitoid rocks. *Geochimica et Cosmochimica Acta* **63**, 1939–1953 (1999).
32. Bockheim, J. G. *Soils of the Laurentian Great Lakes, USA and Canada*. (Springer International Publishing, Cham, 2021). doi:10.1007/978-3-030-52425-8.
33. Jacobs, P. M. & Mason, J. A. Impact of Holocene dust aggradation on A horizon characteristics and carbon storage in loess-derived Mollisols of the Great Plains, USA. *Geoderma* **125**, 95–106 (2005).
34. Cooke, M. J., Stern, L. A., Banner, J. L. & Mack, L. E. Evidence for the silicate source of relict soils on the Edwards Plateau, central Texas. *Quat. res.* **67**, 275–285 (2007).
35. Capo, R. C. & Chadwick, O. A. Sources of strontium and calcium in desert soil and calcrete. *Earth and Planetary Science Letters* **170**, 61–72 (1999).
36. Neff, J. C. *et al.* Increasing eolian dust deposition in the western United States linked to human activity. *Nature Geosci* **1**, 189–195 (2008).
37. Albani, S. *et al.* Paleodust variability since the Last Glacial Maximum and implications for iron inputs to the ocean. *Geophysical Research Letters* **43**, 3944–3954 (2016).
38. Muhs, D. R. & Bettis, E. A. Geochemical Variations in Peoria Loess of Western Iowa Indicate Paleowinds of Midcontinental North America during Last Glaciation. *Quat. res.* **53**, 49–61 (2000).
39. Ratajczak, Z., Nippert, J. B., Briggs, J. M. & Blair, J. M. Fire dynamics distinguish grasslands, shrublands and woodlands as alternative attractors in the C entral G reat P lains of N orth A merica. *Journal of Ecology* **102**, 1374–1385 (2014).

40. Staver, A. C., Archibald, S. & Levin, S. Tree cover in sub-Saharan Africa: Rainfall and fire constrain forest and savanna as alternative stable states. *Ecology* **92**, 1063–1072 (2011).
41. FAO/UNESCO. FAO Soil map of the world. (1974).
42. Slessarev, E. W., Feng, X., Bingham, N. L. & Chadwick, O. A. Landscape Age as a Major Control on the Geography of Soil Weathering. *Global Biogeochem. Cycles* **33**, 1513–1531 (2019).
43. Haines, M., Fishback, P. & Rhode, P. United States Agriculture Data, 1840 - 2012: Version 4. ICPSR - Interuniversity Consortium for Political and Social Research https://doi.org/10.3886/ICPSR35206.V4 (2014).
44. West, T. O. & McBride, A. C. The contribution of agricultural lime to carbon dioxide emissions in the United States: dissolution, transport, and net emissions. *Agriculture, Ecosystems & Environment* **108**, 145–154 (2005).
45. Kim, J. H., Jobbágy, E. G., Richter, D. D., Trumbore, S. E. & Jackson, R. B. Agricultural acceleration of soil carbonate weathering. *Glob. Change Biol.* **26**, 5988–6002 (2020).
46. Raza, S. *et al.* Dramatic loss of inorganic carbon by nitrogen-induced soil acidification in Chinese croplands. *Global Change Biology* **26**, 3738–3751 (2020).
47. Zamanian, K., Zarebanadkouki, M. & Kuzyakov, Y. Nitrogen fertilization raises CO_2 efflux from inorganic carbon: A global assessment. *Global Change Biology* **24**, 2810–2817 (2018).
48. Taylor, L. L. *et al.* Enhanced weathering strategies for stabilizing climate and averting ocean acidification. *Nature Clim Change* **6**, 402–406 (2016).
49. Liu, Z. *et al.* Large and active CO2 uptake by coupled carbonate weathering. *Earth-Science Reviews* **182**, 42–49 (2018).

50. Paradelo, R., Virto, I. & Chenu, C. Net effect of liming on soil organic carbon stocks: A review. *Agriculture, Ecosystems & Environment* **202**, 98–107 (2015).
51. Sokol, N. W. *et al.* Reduced accrual of mineral-associated organic matter after two years of enhanced rock weathering in cropland soils, though no net losses of soil organic carbon. *Biogeochemistry* **167**, 989–1005 (2024).
52. Steinwidder, L. *et al.* Beyond Inorganic C: Soil Organic C as a Key Pathway for Carbon Sequestration in Enhanced Weathering. *Global Change Biology* **31**, e70340 (2025).
53. Xu, T. *et al.* Enhanced Rock Weathering Promotes Soil Organic Carbon Accumulation: A Global Meta-Analysis Based on Experimental Evidence. *Global Change Biology* **31**, e70483 (2025).
54. Tsao, S. S.-E. *et al.* A spatially explicit dataset of agriculture liming across the contiguous United States. Preprint at https://doi.org/10.5194/essd-2025-411 (2025).
55. Soil Survey Staff. Gridded National Soil Survey Geographic (gNATSGO) Database for the Conterminous United States.
56. Gelman, A. Scaling regression inputs by dividing by two standard deviations. *Statistics in Medicine* **27**, 2865–2873 (2008).
57. Labaz, B., Hartemink, A. E., Zhang, Y., Stevenson, A. & Kabała, C. Organic carbon in Mollisols of the world − A review. *Geoderma* **447**, 116937 (2024).
58. Yu, Q. *et al.* A cultivated planet in 2010 – Part 2: The global gridded agricultural-production maps. *Earth Syst. Sci. Data* **12**, 3545–3572 (2020).
59. FAO. Annex I: Food Composition Tables.

60. Bonten, L. T. C., Reinds, G. J. & Posch, M. A model to calculate effects of atmospheric deposition on soil acidification, eutrophication and carbon sequestration. *Environmental Modelling & Software* **79**, 75–84 (2016).
61. Bertagni, M. B., Calabrese, S., Cipolla, G., Noto, L. V. & Porporato, A. Advancing Enhanced Weathering Modeling in Soils: Critical Comparison With Experimental Data. *J Adv Model Earth Syst* **17**, e2024MS004224 (2025).
62. Lembrechts, J. J. *et al.* Global maps of soil temperature. *Global Change Biology* **28**, 3110–3144 (2022).
63. Beck, H. E., De Roo, A. & Van Dijk, A. I. J. M. Global Maps of Streamflow Characteristics Based on Observations from Several Thousand Catchments*. *Journal of Hydrometeorology* **16**, 1478–1501 (2015).
64. Martens, B. *et al.* GLEAM v3: satellite-based land evaporation and root-zone soil moisture. *Geosci. Model Dev.* **10**, 1903–1925 (2017).
65. Zhao, M., Running, S., Heinsch, F. A. & Nemani, R. MODIS-Derived Terrestrial Primary Production. in *Land Remote Sensing and Global Environmental Change* (eds Ramachandran, B., Justice, C. O. & Abrams, M. J.) vol. 11 635–660 (Springer New York, New York, NY, 2010).
66. Swaney, D. P., Howarth, R. W. & Hong, B. Nitrogen use efficiency and crop production: Patterns of regional variation in the United States, 1987–2012. *Science of The Total Environment* **635**, (2018).
67. Schwede, D. B. & Lear, G. G. A novel hybrid approach for estimating total deposition in the United States. *Atmospheric Environment* **92**, 207–220 (2014).

68. Haario, H., Laine, M., Mira, A. & Saksman, E. DRAM: Efficient adaptive MCMC. *Stat Comput* **16**, 339–354 (2006).
69. Soetaert, K. & Petzoldt, T. Inverse Modelling, Sensitivity and Monte Carlo Analysis in *R* Using Package **FME**. *J. Stat. Soft.* **33**, (2010).
70. Prism Climate Group, Oregon State University. Prism climate data. (2011).
71. DiCiccio, T. J. & Efron, B. Bootstrap confidence intervals. *Statist. Sci.* **11**, (1996).
72. Brady, N. C. & Weil, R. R. *The Nature and Properties of Soils*. (Pearson, Harlow, England London New York, 2016).

Supplemental Information: Calcium promotes carbon-rich grassland soils

Slessarev, E.W.,[1,2*] Goertzen, H.R.,[3] Lybrand, R.,[3] McFarlane, K.J.,[4] Pett-Ridge, J.[4,5,6], Sokol, N.[4], Zaharescu, D.[3] Georgiou, K.,[7]

[1] Department of Ecology and Evolutionary Biology, Yale University, New Haven, CT, USA
[2] Yale Center for Natural Carbon Capture, Yale University, New Haven, CT, USA
[3] Department of Land Air and Water Resources, University of California, Davis, CA, USA
[4] Physical and Life Sciences Directorate, Lawrence Livermore National Laboratory, Livermore, CA, USA
[5] Innovative Genomics Institute, University of California Berkeley, Berkeley, CA, USA.
[6] Life & Environmental Sciences Department, University of California Merced, Merced, CA, USA.
[7] Department of Biological and Ecological Engineering, Oregon State University, Corvallis, OR, USA

*Corresponding author: eric.slessarev@yale.edu

Contents:

Supplemental Text: Geochemical model description

Governing equations

Our model was specified to track inputs and outputs of seven ions that control soil pH and weathering rates: Ca^{2+}, Mg^{2+}, Na^{+}, K^{+}, SO_4^{2-}, NO_3^{-}, Cl^{-} (Table S3). These ions were sourced from dissolution of silicate and carbonate minerals, atmospheric deposition, agricultural inputs, and biological fixation in the case of N. Inputs of ions from deposition and ag-lime were treated as instantaneous (i.e., kinetics of lime dissolution were not explicitly modeled). Ions were lost via leaching, secondary mineral precipitation, export in crop biomass, and volatilization in the case of N. Additional ions were assumed to equilibrate instantaneously with the soil solution and hence were modeled implicitly as a function of other factors: H^{+}, Al^{3+}, $Al(OH)^{2+}$, $Al(OH)_2^{+}$, AlH_2Org^{2+}, $AlHOrg^{+}$, OH^{-}, CO_3^{-}, HCO_3^{-}, H_2Org^{-}, $HOrg^{2-}$, Org^{3-}, $Al(OH)_4^{-}$. Apart from export in crop biomass, nutrient uptake and return via litterfall were assumed to be in equilibrium; hence chemical dynamics caused by net growth or mortality of non-agricultural ecosystems were not considered in this study.

Hydrology

We parametrized leaching rates for major ions as a function of recharge or hydrologic baseflow (RC, mm y^{-1}), which we assume represents the flux of water that infiltrates the soil without being lost to evapotranspiration or overland flow. We set a minimum recharge value of 1 mm y^{-1} because zero-recharge values yielded undefined values in the model. After constraining recharge, we partitioned the total amount of soil water (V, l) into mobile and immobile components, under the assumption that only a fraction of the soil pores are leached during leaching events. The immobile component of the soil water was equal to the water content at wilting point (V_{wp}, l), which governed the fraction of soil water mobilized during recharge:

776 $F_{mob} = (V - V_{wp})/V$ (Equation 1)

777 We assumed that only the solutes in the mobile fraction are vulnerable to leaching loss and that
778 solutes are partitioned into mobile and immobile fractions by F_{mob}. We also assumed that solutes
779 in the mobile fraction are conservatively diluted at the timescale of recharge events. The
780 concentration of solute i leached during recharge events (C_i) was therefore a function of the soil
781 moisture at field capacity, V_{fc}:

782 $C_i = M_i * F_{mob}/(V_{fc} - V_{wp})$ (Equation 2)

783 Where M_i was the total moles of the solute in the soil. The leaching rate for a given ion, L_i (mol
784 y^{-1}) was a function of concentration in recharge water (mol l^{-1}) times recharge (l y^{-1}):

785 $L_i = RC * C_i$ (Equation 3)

786 **Weathering kinetics**

787 Weathering kinetic expressions vary widely in complexity. We adopted a simple power law
788 description for silicate weathering kinetics. More complex approaches, such as transition state
789 theory, incorporate multiple reaction mechanisms. These approaches are sensitive to assumptions
790 regarding the type and reactivity of secondary minerals and the extent of mineral surface
791 passivation, which we could not parametrize at the scale of the USA. To further reduce
792 complexity, dissolution kinetics of tectosilicates and inosilicates were referenced to the reactivity
793 of plagioclase feldspar based on a compilation of field-based weathering rate measurements.[1]
794 This was not possible for pyroxene given a lack of field based weathering rate estimates, so we
795 assigned this mineral a reaction rate of 1.0 relative to plagioclase. For tecto- or inosilicate
796 mineral i, weathering rates in the top 100 cm of soil (mol y^{-1}) were a function of total geometric
797 surface area (A_i, m^2), a reaction rate coefficient (r_1, mol m^{-2} y^{-1}), the ratio giving reaction rate

relative to plagioclase (RR_i, unitless), an Arrhenius-type term governing temperature dependence (T_f, unitless), volumetric water content (θ m^3 m^{-3}), the hydrogen ion concentration ($[H^+]$), a reference hydrogen ion concentration ($[H^+_r]$, set equal to 10^{-5}), and the reaction order with respect to H^+ (n).

$$W_i = r_1 * A_i * RR_i * T_f * \theta * (H^+/H^+_r)^n \quad \text{(Equation 4)}$$

For phyllosilicate minerals, the rate expression was identical except that the term RR_i was omitted and an affinity term was added to make the reactions reversible, allowing clay synthesis.

$$W_{i,\,phyllo} = r_2 * A_i * T_f * \theta * (H^+/H^+_r)^n * (1 - \Omega_i) \quad \text{(Equation 5)}$$

The term r_2 gives a reaction rate coefficient for phyllosilicates. The parameter Ω_i was the saturation index for phyllosilicate mineral i, where $\Omega_i = IAP_i/K_{sp}$. The IAP was the ion activity product or reaction quotient. K_{sp} was the solubility constant for each mineral.

We assumed that the temperature and pH dependence of silicate weathering was the same for all minerals. The activation energy for silicate weathering was set to equal 74 kJ mol^{-1} K^{-1}.[2] The temperature modifier for silicate weathering was given by the following equation:

$$T_f = \exp(-Ea_{sil}/R * (1/(T) - 1/(T_{ref}))) \quad \text{(Equation 6)}$$

Where Ea_{sil} was the activation energy for silicates, R was the universal gas constant, T was the soil temperature (K) and T_{ref} was a reference temperature (298 K).

We assigned several silicate weathering parameters manually in order to match published compilations of field weathering rates.[3,4] The parameter r_1 represented the bulk plagioclase feldspar weathering rate coefficient (y^{-1}) at a reference pH of 5.0 ($H_{ref} = 10^{-5}$). We assumed that under the wettest climate conditions, mean soil pH approaches a value of 5.0,[5] and so bulk

819 feldspar weathering rates ought to approach r_1 under these conditions. Across our calibration
820 dataset, the 95th percentile value for recharge (RC) equaled 474 mm, which implies that r_1 equals
821 $10^{-4.3}$ based on the power law relationship between recharge and bulk weathering rates reported
822 by Yu and Hunt (2018).[4] Based on similar reasoning, we set the reaction order for H^+, n, equal to
823 0.66. We chose this value because field estimates of silicate weathering rates increase by roughly
824 two orders of magnitude in the transition from dry conditions (infiltration rates ~ 0.1 m y^{-1}) to
825 humid conditions (infiltration rates ~ 1 m y^{-1}),[3] and soil pH spans roughly 3 units in the transition
826 from wet to dry climates.[5] This implies that weathering rates should increase by two orders of
827 magnitude over a three order of magnitude range in pH (reaction order = 0.66). This value is
828 reasonable for many silicates,[6] and allowed us to recover the observed relationship between
829 feldspar weathering rates in the field and infiltration reasonably well with the calibrated model
830 (Figure S5).

831 We modeled carbonate weathering kinetics using a more complex expression based on
832 transition state theory because carbonate minerals dissolve and precipitate congruently in soil,
833 reducing uncertainty regarding secondary minerals and surface passivation. Dissolution and
834 precipitation for carbonate minerals was governed by the following equation:

835 $$W_{i,\,carb} = r_3 * A_i * \theta * (R_{acid} * [H^+]^{nH} + R_{neutral} + R_{CO2} * pCO_2^{nCO2}) * (1 - \Omega_i) \qquad \text{(Equation 7)}$$

836 Where A_i was the total surface area for mineral i, r_3 was ratio of reactive surface area to
837 geometric surface area for carbonates, R_{acid}, $R_{neutral}$, and R_{CO2} were separate reaction mechanisms
838 for acid, neutral, and CO_2 driven dissolution reactions, nH was the reaction order for H^+, and
839 nCO_2 was the reaction order for CO_2. The parameter Ω_i was the saturation index for carbonate
840 mineral i, where $\Omega_i = IAP_i/K_{sp}$. The IAP was the ion activity product or reaction quotient. K_{sp}

was the solubility constant for each mineral. Reaction mechanisms (R_m) were governed by equations with the form:

$$R_m = A_m * \exp(-Ea_m/R * (1/(T) - 1/(T_{ref}))) \quad \text{(Equation 8)}$$

Where A_m and Ea_m were the preexponential factor (mol m^{-2} y) and activation energy (kJ mol^{-1} K^{-1}) for mechanism m.

All spatially invariant parameters related to weathering reactions are given in Table S5. Our treatment of weathering kinetics left two unknown parameters: r_2, the reaction rate coefficient for phyllosilicates, and r_3, the ratio of reactive to total surface area for carbonates. These parameters were obtained by model inversion (see Methods in main article).

Mineral surface areas

We estimated geometric surface areas for each mineral. For tectosilicates, inosilicates, and carbonates, we assumed that particles were silt- and sand-sized and spherical. We calculated surface area to volume ratios (SVR, m^2 m^{-3}) for silt and sand:

$$SVR = (4 * \pi * (D/2)^2)/(4/3 * \pi * (D/2)^3) \quad \text{(Equation 9)}$$

Where D was the particle diameter, which we set to the geometric mean of each size class.[7] The average surface area to volume ratio for minerals in the silt and sand fraction was then calculated as a weighted average based on silt and sand percentages derived from the NATSGO database (see below). Clays (illite and chlorite) were modeled as cylindrical plates with a diameter of 1 um and a diameter to height ratio of 10:1 [7]

$$SVR_{clay} = ((D/10 * 2 * \pi * D/2) + (2 * \pi * (D/2)^2))/((D/10) * (\pi * (D/2)^2)) \quad \text{(Equation 10)}$$

Total geometric surface area for each mineral was obtained by multiplying the surface area to volume ratio by the total volume of each mineral in the soil.

$A_i = SVR_i * P_i * (\rho_s/\rho_i) * h * 10^{-5}$ (Equation 11)

Where P_i was the percentage of mineral i in the soil, ρ_s was the bulk density of the soil, ρ_i was the density of mineral i, and h was the soil thickness in mm. Chemical formulas and densities for the minerals that we included in the model are shown in Table S6. For clay minerals, we limited our analysis to chlorite (clinochlore) and illite (approximated as muscovite), which we treated as generalized categories that stand in for the full diversity of Mg- and K-bearing 2:1 phyllosilicates (e.g. vermiculite and smectite group clays).

Equilibrium chemistry

We parametrized a set of major equilibrium reactions that governed carbonate ion speciation, aluminum hydrolysis, organic acid speciation, Al-organo ion pair formation, and cation exchange reactions (Table S7). When possible, we obtained equilibrium constants by calculating them from standard enthalpies and entropies, which we obtained from the SUPCRT92 thermodynamic database[8] loaded with the R package CHNOSZ.[9]

Carbonate equilibria depended on the average soil pCO_2, which we parametrized as a function of soil respiration:[10]

$pCO_2 = pCO_{2atm} + 1.03 * Rs/T^2$ (Equation 12)

Where pCO_{2atm} was atmospheric pCO_2, set to 380 ppm for 2001-2010[[11]] and 280 ppm for preindustrial times,[12] and R_s was soil respiration in g m^{-2} y^{-1}. We obtained R_s from net primary productivity (NPP, g m^{-2} y^{-1}):[13]

$R_s = 1.24 * NPP + 24.5$ (Equation 13)

We modeled dissolution and precipitation of carbonates and phyllosilicates as reversible processes governed by chemical equilibria (Table S7), which defined the saturation index (Ω) used in weathering rate calculations. In the case of phyllosilicates, the saturation state depended on dissolved SiO_2, which we did not model explicitly as a state variable. Instead, the concentration of $SiO_{2(aq)}$ was assumed to be determined by instantaneous dissolution and precipitation of amorphous SiO_2 (Table S7).

We represented organic acid speciation using the triprotic model and allowed for formation of ion pairs between Al^{3+} and organic acids. Equilibrium constants for these reactions were obtained by averaging published values from New England lakes, streams, and soils.[14] To parametrize equilibrium reactions involving organic acids, we estimated the amount of dissolved organic carbon and then calculated total organic acid charge (Org_{tot}, moles charge) from total DOC (moles). We converted DOC to Org_{tot} based on a charge density ($m = 0.049$ mol mol^{-1}) averaged from the New England water survey.[14] We approximated soil DOC concentrations by assuming that DOC inputs (I_{DOC}, moles m^{-2} y^{-1}) are equal to NPP, reasoning that over the long run all plant inputs to soil must be converted to DOC before they are respired or sequestered. We then assumed that DOC decays as a first order process and is lost due to leaching:

$$dDOC/dt = I_{DOC} - k_{DOC}*Q_{10}^{((T-293)/10)}*DOC - DOC*RC*F_{mob}/(V_{fc} - V_{wp}) \quad \text{(Equation 14)}$$

Where k_{DOC} was a decay constant and Q_{10} defined the temperature dependence of DOC decay. We obtained k_{DOC} by taking the geometric mean of previously reported "fast" and "slow" DOC decay constants.[15] Assuming that DOC is maintained at steady state for our purposes, the organic acid concentration (molc l^{-1}) was obtained from the following equation:

$$Org_{tot} = m*(I_{DOC})/(1 + k_{DOC}*Q_{10}^{((T-293)/10)})*(1/V) \quad \text{(Equation 15)}$$

905 Exchange reactions were specified using the Gaines-Thomas approach. We parameterized
906 cation exchange reactions using an existing compilation,[16] which summarized Gaines-Thomas
907 exchange constants for sand, loess (silt enriched), and clay dominated soils in the Netherlands.
908 As a first order approximation, we assigned exchange constants by calculating the weighted
909 mean of the profile-averaged constants listed in the compilation, with weights given by the sand,
910 silt, and clay fractions obtained from NATSGO.

911 When calibrating the model, we simulated re-equilibration of soil pH with laboratory
912 conditions because in-situ pH and laboratory-measured pH can vary substantially.[17] To do this,
913 we fixed soil water content so that the soil mass to water ratio equaled 1:1, set the temperature to
914 20°C, and adjusted pCO_2 to reflect the ambient atmospheric concentration. Concentrations of
915 conserved ions were adjusted to reflect the change in soil water content during measurement.
916 Charge balance and exchange reactions were solved based on laboratory parameters to yield
917 laboratory pH. In cases where the soil contained calcite, we assumed that calcite could partially
918 buffer pH at the timescale of laboratory measurement. This assumption is supported by a global
919 pH compilation, which shows that pH approximates a calcite-buffered value when carbonates are
920 present in even small amounts.[5] To represent carbonate buffering in the lab, we fixed the
921 saturation index for calcite so that it would equal its value in the field and then solved for the
922 equilibrium Ca concentration at the laboratory pCO_2 and temperature.

923 **Nutrient budgets**

924 While our main goal was to model pre-agricultural Ca weathering across the USA, we
925 considered nutrient inputs and outputs in modern croplands to assist with model calibration and
926 to help us understand how Ca fluxes have changed over time. Nitrogen had the most complex
927 nutrient budget. To simplify N accounting, we assumed that all reduced N is completely nitrified

following DON export; hence all N is treated as NO_3^-.[18] In natural systems, the only N inputs in the model were atmospheric deposition and nitrogen fixation (F_N, mol m^{-2} y^{-1}), which we modeled as a function of NPP:[19]

$$F_N = 1.8*(1 - \exp(-0.003*NPP))/14.01 \quad \text{(Equation 16)}$$

In addition to leaching of NO_3^-, we considered leaching of organic N, which we assume happens before nitrification. We assigned a molar CN ratio of 20, which is typical for dissolved organic matter,[20] and modeled DON export as a function of DOC leaching:

$$L_N = N*RC*F_{mob}/(V_{fc} - V_{wp}) + DOC/CN_{DOM}*RC*F_{mob}/(V_{fc} - V_{wp}) \quad \text{(Equation 17)}$$

Because we fixed the CN ratio for DOM, DON export could exceed inputs, leading to negative NO_3^- concentrations. In these cases, we forced DON export to equal inputs and NO_3^- concentrations equaled zero.

In croplands, natural N fixation was set to zero and we considered N inputs from fertilizer, manure, crop N fixation, free living N fixation, and N removal in crop biomass:

$$C_N = N_{fert} + N_{man} + N_{fix,crop} + N_{fix,free} - N_{rem} \quad \text{(Equation 18)}$$

The first three of these parameters as well as the N removal rate varied spatially and were taken from a published county-level compilation[21] whereas free-living N fixation rates were approximated at 0.036 mol m^{-2} y^{-1}[22] and did not vary spatially. The parameter N_{man} was set equal to 20% of total manure N to account for inefficiency in manure recovery.[23]

Nitrogen can be lost from soil via ammonia volatilization, NO_x emission, and denitrification to N_2O or N_2. The processes governing these fluxes are complex and representing

them in detail was beyond the scope of our effort. Instead, we manually calibrated a single parameter, r_v, that controlled the N volatilization rate:

$$V_N = N/N_{inputs} * r_v \qquad \text{(Equation 19)}$$

The expression was based on the assumption that N volatilization is proportional to the total available N pool but inversely proportional to N inputs. We reasoned that as N inputs increase, the opportunity for denitrification and ammonia volatilization would be lower because more N would escape the soil before volatilization. This is consistent with the observation that low-input ecosystems volatilize a greater fraction of N than high-input agricultural systems.[24] We selected a value of 0.3 y^{-1} for r_v, which ensured plausible nitrate stocks for the top 1 meter of soil: in the range of 100-200 kg NO_3^--N ha^{-1} in croplands[25,26] and less than 10 kg NO_3^--N ha^{-1} in forests.[27]

Nitrogen removal in harvest could sometimes exceed N inputs, leading to implausibly low NO_3^- concentrations. At locations where N surplus in croplands was less than 0.1 mol m^{-2} y^{-1}, we assumed that imbalances in the N budget were being met by an unknown source (e.g., decomposition of soil organic matter or higher than 20% manure recoverability). In these cases, we assigned a minimum value of 0.1 mol m^{-2} y^{-1} for the net nitrogen balance before applying losses from NO_3^- leaching and volatilization. This minimum value maintained cropland NO_3^- levels within reported ranges. [25,26]

Cropland C budgets were also adjusted to account for import and export of C in agriculture. We adjusted NPP in croplands to account for removal of crop biomass, which accounts for 43% of cropland NPP.[28] We also accounted for C introduced with manure. We assumed a molar C:N ratio of 10 for manure, and used this number to scale manure C based on county-level estimates for manure N.

We also considered cropland nutrient budgets for some additional nutrients. For simplicity, we assumed that S and K inputs in fertilizer equaled outputs; hence C_S and C_K were set equal to zero. For Ca and Mg, we accounted for inputs in manure and ag-lime and outputs in crop harvest. Manure inputs were constrained by assigning Ca:N and Mg:N values for manure and scaling Ca and Mg inputs to the manure N application rate. Ca:N and Mg:N for manure were averaged across dairy solids, swine solids, and poultry manure types.[29] Similarly, average Ca:N and Mg:N values were assigned for crop biomass using published values for corn and soy,[30] allowing us to approximate Ca and Mg removal in harvest.

We modeled liming rates endogenously as a function of pH. We first aligned county level liming data from 1987[[31]] (the most recent available date) with maps of soil pH derived from NATSGO.[32] We assigned a pH value to croplands in each county by extracting NATSGO pH values in a 10 km grid across the USA and masking out non-cropland areas using the GFSAD cropland mask.[33] We then calculated the median cropland pH value in each county. This revealed that liming rates vary widely below pH 7, but are low above pH 7. We modeled the maximum rate of lime addition as a function of pH using a sigmoid function:

$$Lime_{max} = p_1*(1-\exp(-10^{-pHlab}/p_2)^{p3}) \qquad \text{(Equation 20)}$$

Where $Lime_{max}$ was the maximum observed liming rate (t ha^{-1} y^{-1}) p_1, p_2, and p_3 were empirical constants and pH_{lab} was the laboratory-measured soil pH assumed equal to the median pH from NATSGO. We fit this function to the condition 90th percentiles of the data obtained in 0.5 pH-unit bins using the R function "nls". The parameters received estimated values of p_1 = 0.424, $p_2 = 1.42*10^{-7}$, and p_3 = 1.13.

991 Below the maximum liming rate, we assumed that farmers add enough lime to neutralize
992 acidity from fertilizer and replace Ca and Mg lost in crop biomass. Consequently, the main effect
993 of liming in the model was to maintain soil pH at the same level it would have attained under
994 unfarmed conditions. We made this assumption because it was a reasonable compromise between
995 two extreme alternatives: (1) assuming that farmers generally add lime aggressively to raise their
996 soil pH to agronomically optimal levels; or (2) farmers generally do not add enough lime to
997 maintain soil pH, and croplands are broadly acidified compared to unfarmed baseline conditions.
998 To estimate the liming rate, we first ran the model without agricultural influence, which yielded
999 the target pH value, pH_{target}. We then modeled lime addition as a function of pH_{lab} that increases
1000 steeply towards $Lime_{max}$ at pH_{target}:

1001 $$Lime_{tot} = Lime_{max} * (1-\exp(-10^{-pHlab}/10^{-pHtarget})^{20}) \qquad \text{Equation 21}$$

1002 Applying this equation required approximating pH_{lab} because the model was designed to
1003 calculate the in-situ field pH, while laboratory pH was estimated as a post-processing step at
1004 some computational cost. To address this, we derived empirical linear relationships between the
1005 in-situ pH and the laboratory pH prior to running cropland simulations, with a separate
1006 relationship fitted for carbonate-buffered and carbonate free soils. These regressions explained
1007 >90% of the variation in pH_{lab} and could be used to solve Equation 21 without explicitly
1008 estimating this quantity at every model iteration, speeding up computations substantially.

1009 After applying Equation 21, we partitioned lime added into calcitic and dolomitic
1010 components. In general, crop Mg removal exceeded inputs, and so we satisfied Mg demand first.
1011 Mg demand (mol m^{-2} y^{-1}) was set equal to the cropland partial Mg budget (crop removal –
1012 manure inputs) where removal exceeded inputs and set to zero elsewhere. Dolomitic lime
1013 addition (mol m^{-2} y^{-1}) was then set to equal to Mg demand. Where Mg demand could not be met

because the mass of dolomite added exceeded $Lime_{max}$, the cropland Mg budget was set equal to zero and it was assumed the Mg came from other unknown sources. Calcitic lime addition was calculated as the difference between the mass of dolomite added and $Lime_{tot}$. Ca and Mg added in lime were obtained from dolomitic and calcitic lime based on the chemical formulae for calcite and dolomite (Table S6).

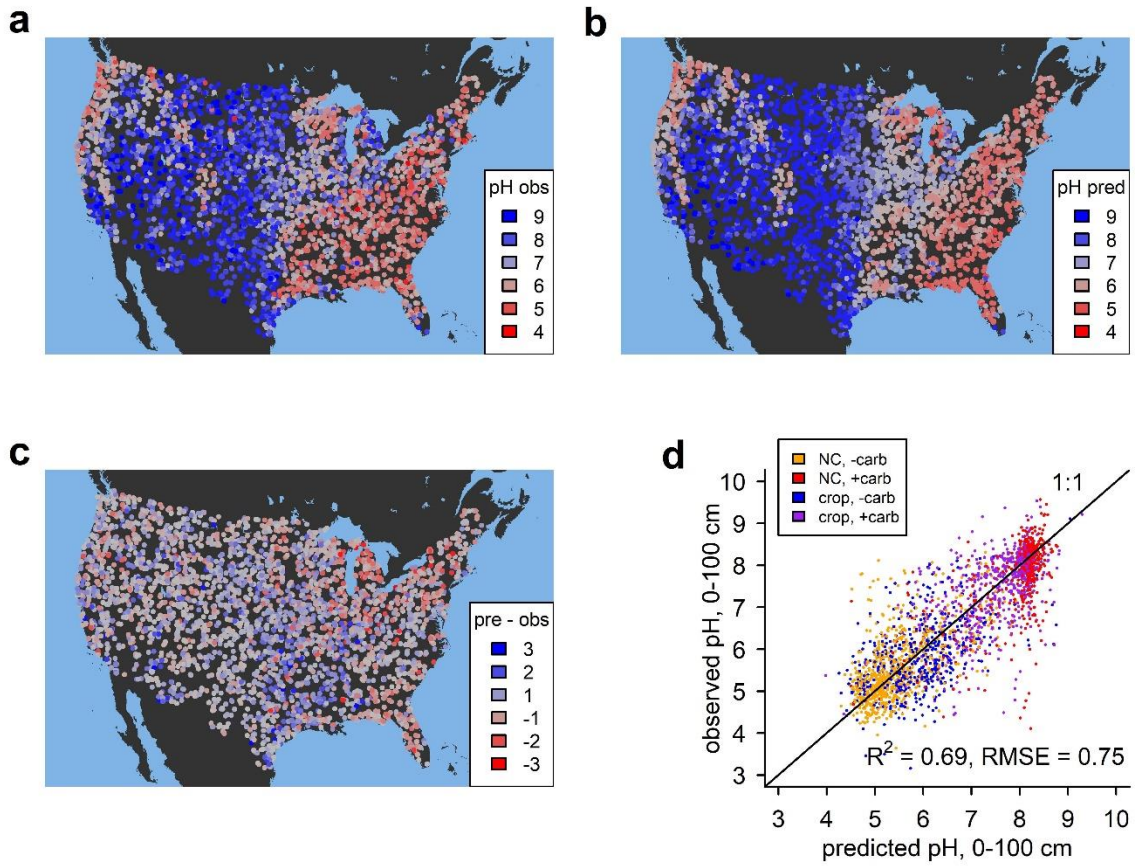

Figure S1. Model performance matching soil pH. (a) shows observed depth-weighted average soil pH of the top 100 cm at 4,247 unique locations used for model training and validation. (b) shows pH simulated by the calibrated model at the same locations, and (c) shows the model residuals (predicted – observed pH). (d) shows a plot of predicted versus observed pH, with colors representing different combinations of land use and soil carbonate status (NC, -carb = non-cropland, carbonate free; NC, +carb = non-cropland, carbonates present; crop, -carb = cropland, carbonate free; crop, +carb = cropland, carbonates present). RMSE is the root mean squared error.

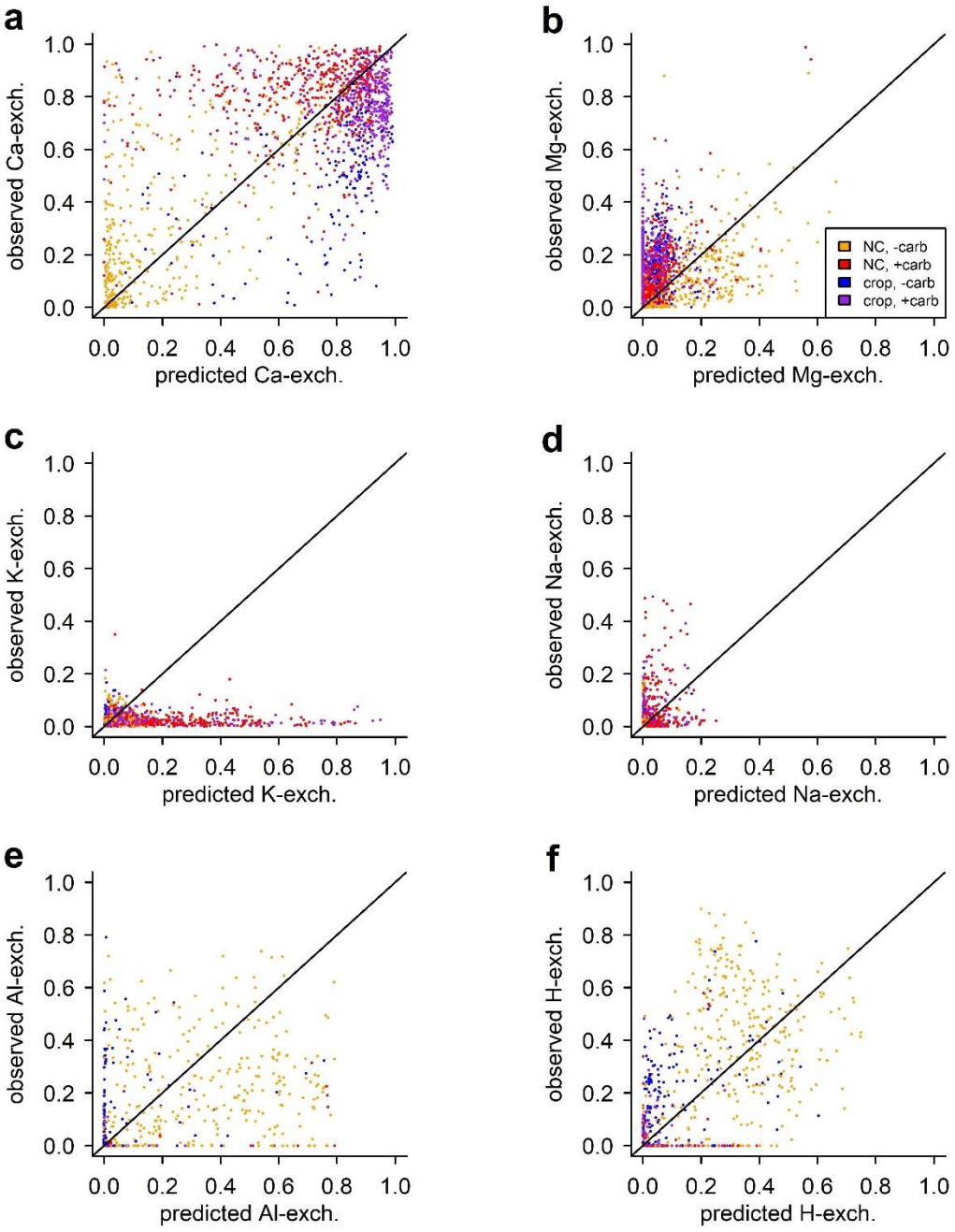

Figure S2. Model performance for exchangeable ions. (a) – (f) show predicted versus observed exchange fractions for Ca, Mg, K, Na, Al, and H^+. Observed values represent depth-weighted averages to 100 cm taken from the NCSS database[35] (n = 2,563 unique profiles). Values are normalized by total cation exchange capacity (moles cation charge / CEC). Colors represent different combinations of land use and soil carbonate status (NC, -carb = non-cropland, carbonate free; NC, +carb = non-cropland, carbonates present; crop, -carb = cropland, carbonate free; crop, +carb = cropland, carbonates present). Diagonal lines show the 1:1 relationship.

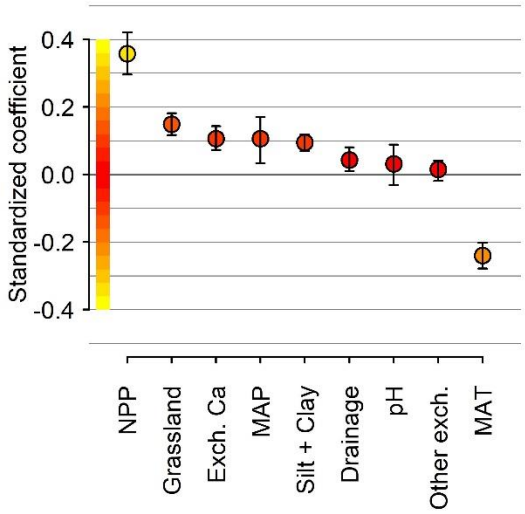

Figure S3. Controls on Mollisol distribution and A-horizon soil organic carbon stocks in the USA with alternative predictors. Standardized regression coefficients were derived from a multivariate linear regression model, where A-horizon organic carbon stocks were predicted as a function of the eight variables listed on the horizonal axis. In (a) exchangeable Ca fraction was included in the regression rather than base saturation as in the main text. In (b) cation exchange capacity was corrected for the contribution from soil organic matter prior to calculating exchangeable ion pools. In both panels, whiskers show 95% confidence intervals derived from a spatial blocked bootstrapping procedure (see Methods). The absolute value of each regression coefficient is an index of how strongly related each variable is to the response variable, and is shown with a relative color scale: yellow = maximum, red = zero. Abbreviations: NPP = net primary productivity, MAT = mean annual soil temperature, MAP = mean annual precipitation, Exch. Ca = total exchangeable Ca, Other exch. = sum of non-Ca exchangeable ions.

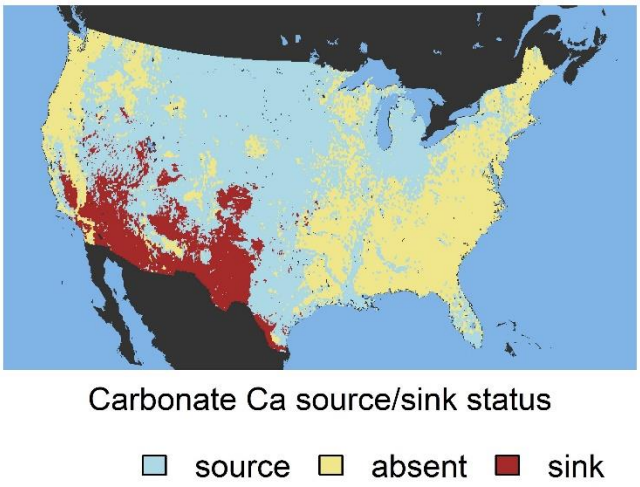

Figure S4. Modeled carbonate source / sink status. Data show model simulations under preindustrial late Holocene conditions. Areas mapped in yellow are carbonate free, areas mapped in blue are releasing Ca via carbonate weathering, and areas mapped in red are a sink for Ca via carbonate formation.

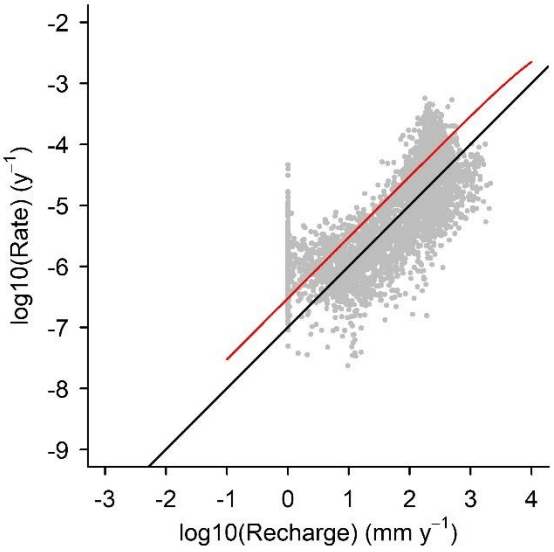

Figure S5. Modeled plagioclase feldspar weathering rate versus recharge. Gray points show modeled feldspar weathering rates normalized by the feldspar stock versus the recharge parameter. The red line shows the non-linear fit to a compilation of field and lab weathering rates from Maher 2010,[3] and the black line shows a fit to the same complication from Yu and Hunt 2018[4].

	R^2	RMSE
Ca^{2+}	0.40	0.26
Mg^{2+}	0.06	0.15
Na^{+}	0.08	0.06
K^{+}	0	0.18
Al^{3+}	0.30	0.15
H^{+}	0.51	0.14
All	0.66	0.17

Table S1. Validation statistics for exchangeable ion fractions. R^2 values are derived by regressing observations on predictions; root mean squared error (RMSE) was calculated as the square root of the mean of the squared residuals (geochemical model predictions – observations). Statistics for all cations were obtained by treating all observed and predicted cation fractions as independent values and pooling them. Observed values represent depth-weighted averages to 100 cm taken from the NCSS database[35] (n = 2,563 unique profiles; 3,423 total including repeats from spatially weighted resampling).

	value	CI
intercept	-0.05	[-0.065, -0.036]
grassland	0.139	[0.106, 0.171]
exch. Ca	0.144	[0.109, 0.178]
other exch.	0.011	[-0.018, 0.039]
MAT	-0.229	[-0.265, -0.188]
silt + clay	0.032	[0.000, 0.065]
Drainage	0.088	[0.062, 0.111]
log NPP	0.347	[0.289, 0.411]
MAP	0.105	[0.030, 0.168]
pH	0.009	[-0.055, 0.064]

Table S2. Results of multiple regression analysis for A-horizon SOC. Statistics are derived from a multivariate logistic regression, where log-transformed A-horizon organic carbon stocks were modeled as a function of potential grassland and savanna vegetation (grassland), exchangeable Ca (Ca exch.), non-Ca exchangeable ions (other exch.), soil silt + clay content, net primary productivity (NPP), USDA drainage class (drainage), Mean annual soil temperature (MAT), and mean annual precipitation (MAP). Continuous predictors were scaled by their standard deviations prior to fitting, whereas the binary predictor (grassland) was scaled by two times its standard deviation. Model $R^2 = 0.30$ and residual standard error was 0.4188. Confidence intervals were derived from a spatially blocked bootstrapping procedure (see Methods).

Ion or algebraic constraint	Equation
Ca^{2+}	$dCa/dt = D_{Ca} + A_{Ca} + C_{Ca} + R_{Cc,Ca} + R_{Do,Ca} + R_{Pl,Ca} + R_{Hb,Ca} + R_{Py,Ca} - L_{Ca}$
Mg^{2+}	$dMg/dt = D_{Mg} + A_{Mg} + C_{Mg} + R_{Do,Mg} + R_{Hb,Mg} + R_{Py,Mg} + R_{Cl,Mg} - L_{Mg}$
Na^{+}	$dNa/dt = D_{Na} + R_{Pl,Na} - L_{Na}$
K^{+}	$dK/dt = D_{K} + C_{K} + M_{K} + R_{Ks,K} + R_{Il,K} - L_{K}$
NO_3^{-}	$dN/dt = D_{N} + C_{N} + F_{N} - V_{N} - L_{N}$
SO_4^{2-}	$dS/dt = D_{S} + C_{S} - L_{S}$
Cl^{-}	$dCl/dt = D_{Cl} - L_{Cl}$
Charge Balance	$0 = (2[Ca^{2+}]+ 2[Mg^{2+}] + [K^{+}] + [Na^{+}] + 3[Al^{3+}] + 2[Al(OH)^{2+}] + [Al(OH)_2^{+}] + 2[AlHOrg^{2+}] + [AlH_2Org^{+}] + [H^{+}]) - ([OH^{-}] + [HCO_3^{-}] + 2[CO_3^{2-}] + [H_2Org^{-}] + 2[HOrg2-] + 3[Org^{3-}] + [Al(OH)_4^{-}] + 2[SO_4^{2-}] + [NO_3^{-}] + [Cl^{-}])$
Exchange	$1 = fCa + fMg + fNa + fK + fAl + fH$

Table S3 Governing equations. Capital letters indicate rates: D = deposition (wet + dry); A = agricultural liming, C = cropland nutrient budget (inputs – uptake); R = weathering; L = leaching; F = fixation; V = volatilization. Weathering rates (mol mineral y^{-1}) were multiplied by the molar concentration of each element the mineral to yield the flux of each element from the mineral; this is indicated in the subscripts, with the mineral listed first and then the corresponding element. Minerals: Cc = calcite; Do = dolomite; Pl = plagioclase; Hb = hornblende; Py = pyroxene; Cl = chlorite; Ks = K-feldspar; Il = illite.

Mineral	Abbr.	Type	Formula	Density
Plagioclase	Pl	tectosilicate	$Na_{(1-fAn)}Ca_{fAn}Al_{(1+fAn)}Si_{(3-fAn)}O_8$	$2.75f_{An} + 2.625(1-f_{An})$
K-feldspar	Ks	tectosilicate	$KAlSi_3O_8$	2.59
Pyroxene	Py	inosilicate	$MgCa(SiO_3)_2$	3.3
Hornblende	Hb	inosilicate	$Ca_2(Mg_2Fe_2Al)Si_7AlO_{22}(OH)_2$	3.1735
Chlorite	Cl	phyllosilicate	$Mg_5Al_2Si_3O_{18}H_8$	2.915
Illite	Il	phyllosilicate	$K(Al_2)(Si_3Al)O_{10}(OH)_2$	2.795
Calcite	Cc	carbonate	$CaCO_3$	2.7102
Dolomite	Do	carbonate	$CaMg(CO_3)_2$	2.85

Table S4 Mineral properties. f_{An} = anorthite molar fraction. Densities are midpoints of reported ranges from Mindat.org.

Parameter	Description	Value	Units	Source
Ea_{sil}	Silicate weathering activation energy	74	kJ mol^{-1} K^{-1}	[2]
Hr	Reference [H+] value	10^{-5}	mol l^{-1}	This study
nH	Silicate weathering reaction order for H+	0.6667	-	This study
RRPl	Relative reaction rate, plagioclase	1	-	[1]
RRKs	Relative reaction rate, K-feldspar	0.63	-	[1]
RRHb	Relative reaction rate, hornblende	0.25	-	[1]
RRPy	Relative reaction rate, pyroxene	1	-	This study
$\log(A_{acid,Cc})$	Acid mechanism preexponential factor, calcite	-0.3	mol m^{-2} s^{-1}	[6]
$\log(A_{neut,Cc})$	Neutral mechanism preexponential factor, calcite	-5.81	mol m^{-2} s^{-1}	[6]
$\log(A_{CO2,Cc})$	CO_2 mechanism preexponential factor, calcite	-3.48	mol m^{-2} s^{-1}	[6]
$\log(A_{acid,Do})$	Acid mechanism preexponential factor, dolomite	-3.19	mol m^{-2} s^{-1}	[6]
$\log(A_{neut,Do})$	Neutral mechanism preexponential factor, dolomite	-7.53	mol m^{-2} s^{-1}	[6]
$\log(A_{CO2,Do})$	CO_2 mechanism preexponential factor, dolomite	-5.11	mol m^{-2} s^{-1}	[6]
$Ea_{acid,cc}$	Acid mechanism activation energy, calcite	14.4	kJ mol^{-1} K^{-1}	[6]
$Ea_{neut,cc}$	Neutral mechanism activation energy, calcite	23.5	kJ mol^{-1} K^{-1}	[6]
$Ea_{CO2,cc}$	CO_2 mechanism activation energy, calcite	35.4	kJ mol^{-1} K^{-1}	[6]
$Ea_{acid,do}$	Acid mechanism activation energy, dolomite	36.1	kJ mol^{-1} K^{-1}	[6]
$Ea_{neut,do}$	Neutral mechanism activation energy, dolomite	52.2	kJ mol^{-1} K^{-1}	[6]
$Ea_{CO2,do}$	CO_2 mechanism activation energy, dolomite	34.8	kJ mol^{-1} K^{-1}	[6]
nH_{Cc}	Reaction order for H^+, calcite	1	-	[6]
$nCO_{2,Cc}$	Reaction order for CO_2, calcite	1	-	[6]
nH_{Do}	Reaction order for H^+, dolomite	0.5	-	[6]
$nCO_{2,Do}$	Reaction order for CO_2, dolomite	0.5	-	[6]

Table S5 Weathering rate parameters

Reaction	ΔS (kJ K^{-1} mol^{-1})	ΔH (kJ mol^{-1})	logK	source
$CO_{2\ (g)} \leftrightarrow CO_{2\ (aq)}$	-0.09617	-20.28822		[8,9]
$CO_{2\ (aq)} + H_2O \leftrightarrow HCO_3^- + H^+$	-0.08905	9.701672		[8,9]
$HCO_3^- \leftrightarrow CO_3^{2-} + H^+$	-0.14845	14.69839		[8,9]
$H_2O \leftrightarrow OH^- + H^+$	-0.08064	55.81354		[8,9]
$Al(OH)_{3\ (s)} \leftrightarrow Al(OH)_{3\ (aq)}$	-0.00909	50.45804		[8,9]
$Al(OH)_{3\ (aq)} + 3H^+ \leftrightarrow Al^{3+} + 3H_2O$	-0.18933	-153.61150		[8,9]
$Al(OH)_{3\ (aq)} + 2H^+ \leftrightarrow Al(OH)_2^+ + 2H_2O$	-0.10063	-98.86893		[8,9]
$Al(OH)_{3\ (aq)} + 1H^+ \leftrightarrow Al(OH)^{2+} + H_2O$	-0.01697	-39.97106		[8,9]
$Al(OH)_{3\ (aq)} + H_2O \leftrightarrow Al(OH)_4^- + H^+$	-0.02573	25.43200		[8,9]
$CaCO_{3\ (s)} \leftrightarrow Ca^{2+} + CO_3^{2-}$	-0.19821	-11.49904		[8,9]
$CaMgC_2O_{6\ (s)} \leftrightarrow Ca^{2+} + Mg^{2+} + 2CO_3^{2-}$	-0.44944	-34.26448		[8,9]
$(1/5)Mg_5Al_2Si_3O_{18}H_{8\ (s)} + 2H^+ \leftrightarrow (2/5)Al(OH)_{3\ (aq)} + Mg^{2+} + (3/5)SiO_{2\ (aq)} + (6/5)H_2O$	-0.072267	-50.73344		[8,9]
$KAl_3Si_3O_{12}H_{2\ (s)} + H^+ + 3H_2O \leftrightarrow 3Al(OH)_{3\ (aq)} + K^+ + 3SiO_{2\ (aq)}$	-0.00210	227.67055		[8,9]
SiO_2(amorph) ↔ SiO_2(aq)	0.01531	20.05391		[8,9]
$H_3Org \leftrightarrow H_2Org^- + H^+$			-2.653	[14]
$H_2Org^- \leftrightarrow HOrg^{2-} + H^+$			-6.233	[14]
$HOrg^{2-} \leftrightarrow Org^{3-} + H^+$			-7.467	[14]
$AlH_2Org^{2+} \leftrightarrow H^+ + AlHOrg^+$			-4.963	[14]
$AlHOrg^+ \leftrightarrow H^+ + AlOrg$			-4.040	[14]
$AlOrg \leftrightarrow Al^{3+} + Org^{3-}$			-10.020	[14]
$3Ca\text{-}X + 2Al^{3+} \leftrightarrow 2Al\text{-}X + 3Ca^{2+}$			2.026 (s); 1.195 (lo); 0.106 (cl)	[16]
$3Mg\text{-}X + 2Al^{3+} \leftrightarrow 2Al\text{-}X + 3Mg^{2+}$			2.811 (s); 1.244 (lo); 0.599 (cl)	[16]
$3Na\text{-}X + Al^{3+} \leftrightarrow Al\text{-}X + 3Na^+$			1.811 (s); 0.646 (lo); 1.045 (cl)	[16]
$3K\text{-}X + Al^{3+} \leftrightarrow Al\text{-}X + 3K^+$			-0.917 (s); -2.413 (lo); -3.561 (cl)	[16]
$3H\text{-}X + Al^{3+} \leftrightarrow Al\text{-}X + 3H^+$			-6.924 (s); -7.532 (lo); -9.923 (cl)	[16]

Table S6 Equilibrium reactions and thermodynamic parameters. For exchange reactions logK values are for sand, loess, and clay respectively based on reference [9].

References

1. White, A. F. & Buss, H. L. Natural Weathering Rates of Silicate Minerals. in *Treatise on Geochemistry* 115–155 (Elsevier, 2014). doi:10.1016/B978-0-08-095975-7.00504-0.
2. West, A., Galy, A. & Bickle, M. Tectonic and climatic controls on silicate weathering. *Earth and Planetary Science Letters* **235**, 211–228 (2005).
3. Maher, K. The dependence of chemical weathering rates on fluid residence time. *Earth and Planetary Science Letters* **294**, 101–110 (2010).
4. Yu, F. & Hunt, A. G. Predicting soil formation on the basis of transport-limited chemical weathering. *Geomorphology* **301**, 21–27 (2018).
5. Slessarev, E. W. *et al.* Water balance creates a threshold in soil pH at the global scale. *Nature* **540**, 567–569 (2016).
6. Palandri & Kharaka, Y. A compilation of rate parameters of water-mineral interaction kinetics for application to geochemical modeling. (2004).
7. Swoboda-Colberg, N. G. & Drever, J. I. Mineral dissolution rates in plot-scale field and laboratory experiments. *Chemical Geology* **105**, 51–69 (1993).
8. Johnson, J. W., Oelkers, E. H. & Helgeson, H. C. SUPCRT92: A software package for calculating the standard molal thermodynamic properties of minerals, gases, aqueous species, and reactions from 1 to 5000 bar and 0 to 1000°C. *Computers & Geosciences* **18**, 899–947 (1992).
9. Dick, J. M. CHNOSZ: Thermodynamic Calculations and Diagrams for Geochemistry. *Front. Earth Sci.* **7**, 180 (2019).
10. Gaillardet, J., Calmels, D., Romero-Mujalli, G., Zakharova, E. & Hartmann, J. Global climate control on carbonate weathering intensity. *Chemical Geology* **527**, 118762 (2019).
11. Lan, X. & Keeling, R. Trends in atmospheric carbon dioxide.

12. Etheridge, D. M. *et al.* Natural and anthropogenic changes in atmospheric CO_2 over the last 1000 years from air in Antarctic ice and firn. *J. Geophys. Res.* **101**, 4115–4128 (1996).
13. Raich, J. W. & Schlesinger, W. H. The global carbon dioxide flux in soil respiration and its relationship to vegetation and climate. *Tellus B* **44**, 81–99 (1992).
14. Fakhraei, H. & Driscoll, C. T. Proton and Aluminum Binding Properties of Organic Acids in Surface Waters of the Northeastern U.S. *Environ. Sci. Technol.* **49**, 2939–2947 (2015).
15. Camino-Serrano, M. *et al.* ORCHIDEE-SOM: modeling soil organic carbon (SOC) and dissolved organic carbon (DOC) dynamics along vertical soil profiles in Europe. *Geosci. Model Dev.* **11**, 937–957 (2018).
16. Vries, W. & Posch, M. Derivation of cation exchange constants for sand, loess, clay and peat soils on the basis of field measurements in the Netherlands. (2003).
17. Kanzaki, Y., Chiaravalloti, I., Zhang, S., Planavsky, N. J. & Reinhard, C. T. In silico calculation of soil pH by SCEPTER v1.0. *Geosci. Model Dev.* **17**, 4515–4532 (2024).
18. Posch, M. & Reinds, G. J. A very simple dynamic soil acidification model for scenario analyses and target load calculations. *Environmental Modelling & Software* **24**, 329–340 (2009).
19. Wieder, W. R., Cleveland, C. C., Lawrence, D. M. & Bonan, G. B. Effects of model structural uncertainty on carbon cycle projections: biological nitrogen fixation as a case study. *Environ. Res. Lett.* **10**, 044016 (2015).
20. Wymore, A. S. *et al.* Gradients of Anthropogenic Nutrient Enrichment Alter N Composition and DOM Stoichiometry in Freshwater Ecosystems. *Global Biogeochemical Cycles* **35**, e2021GB006953 (2021).

21. Swaney, D. P., Howarth, R. W. & Hong, B. Nitrogen use efficiency and crop production: Patterns of regional variation in the United States, 1987–2012. *Science of The Total Environment* **635**, (2018).
22. Smil, V. Nitrogen in crop production: An account of global flows. *Global Biogeochemical Cycles* **13**, 647–662 (1999).
23. Kellogg, R. L., Lander, C. H., Moffitt, D. C. & Gollehon, N. Manure nutrients relative to the capacity of cropland and pastureland to assimilate nutrients: Spatial and temporal trends for the United States. (2000).
24. Velthof, G. L. *et al.* Integrated Assessment of Nitrogen Losses from Agriculture in EU-27 using MITERRA-EUROPE. *J of Env Quality* **38**, 402–417 (2009).
25. Roth, G. W. & Fox, R. H. Soil Nitrate Accumulations following Nitrogen-Fertilized Corn in Pennsylvania. *J of Env Quality* **19**, 243–248 (1990).
26. Ziadi, N., Bélanger, G. & Claessens, A. Relationship between soil nitrate accumulation and in-season corn N nutrition indicators. *Can. J. Plant Sci.* **92**, 331–339 (2012).
27. Xu-Ri & Prentice, I. C. Terrestrial nitrogen cycle simulation with a dynamic global vegetation model. *Global Change Biology* **14**, 1745–1764 (2008).
28. West, T. O., Bandaru, V., Brandt, C. C., Schuh, A. E. & Ogle, S. M. Regional uptake and release of crop carbon in the United States. *Biogeosciences* **8**, 2037–2046 (2011).
29. Animal Manure Production and Utilization in the US. in *Applied Manure and Nutrient Chemistry for Sustainable Agriculture and Environment* 1–21 (Springer Netherlands, Dordrecht, 2014). doi:10.1007/978-94-017-8807-6_1.

30. Masters, M. D. *et al.* Soil nutrient removal by four potential bioenergy crops: Zea mays, Panicum virgatum, Miscanthus×giganteus, and prairie. *Agriculture, Ecosystems & Environment* **216**, 51–60 (2016).
31. Haines, M., Fishback, P. & Rhode, P. United States Agriculture Data, 1840 - 2012: Version 4. ICPSR - Interuniversity Consortium for Political and Social Research https://doi.org/10.3886/ICPSR35206.V4 (2014).
32. Soil Survey Staff. Gridded National Soil Survey Geographic (gNATSGO) Database for the Conterminous United States.
33. Teluguntla, P. *et al.* NASA Making Earth System Data Records for Use in Research Environments (MEaSUREs) Global Food Security Support Analysis Data (GFSAD) Crop Mask 2010 Global 1 km V001. NASA Land Processes Distributed Active Archive Center https://doi.org/10.5067/MEASURES/GFSAD/GFSAD1KCM.001 (2016).
34. West, T. O. & McBride, A. C. The contribution of agricultural lime to carbon dioxide emissions in the United States: dissolution, transport, and net emissions. *Agriculture, Ecosystems & Environment* **108**, 145–154 (2005).
35. National Cooperative Soil Survey. National Cooperative Soil Survey Soil Characterization Database. (2018).